Study of temperature effect on hydrogen embrittlement in X70 pipeline steel

Xiao Xing [a,b,*], Zhiwen Pang [a,b], Hao Zhang [c,**], Jianguo Liu [a,b], Gan Cui [a,b]

[a] College of Pipeline and Civil Engineering, China University of Petroleum (East China), Qingdao 266580, China
[b] Shandong Key Laboratory of Oil & Gas Storage and Transportation Safety, Qingdao 266580, China
[c] Department of Chemical and Materials Engineering, University of Alberta, Edmonton, AB T6G 1H9, Canada

ARTICLE INFO

ABSTRACT

The study investigates the temperature effect on hydrogen embrittlement (HE) in X70 steel using Devanathan-Stachurski and tensile tests under varying cathodic hydrogen-charging currents. The most severe HE temperature threshold is identified via scanning electron microscope (SEM) and electron backscatter diffraction (EBSD) methods. The temperature thresholds for 10 mA/cm^2 and 20 mA/cm^2 are 293 K and 283 K, respectively, while no critical temperature at 30 mA/cm^2. The underlying mechanism is studied, and a predictive model is established. Also, the primary hydrogen-induced fracture plane is identified as {110}, beneath where hydrogen enhances plastic deformation in {110}<111> and inhibits in {112}<111>.

1. Introduction

Pipeline transportation can achieve low-cost and large-scale hydrogen energy supply. Especially, the hydrogen could be transported by blending it into natural gas through the application of the existing natural gas transmission pipeline [1,2]. However, HE is the most severe degradation mechanism of pipeline steel in hydrogen transmission. Many factors affect the HE of pipeline steel, including the metallurgical properties and environmental effects. Among them, the temperature effect is the most complicated. Typically, the temperature increment can enhance HE by increasing hydrogen atom generation on the steel surface and facilitating the diffusion of hydrogen [3]. However, the temperature softening effect on steel indicates that the fracture toughness of pipeline steel should increase with temperature. These controversial results make the temperature susceptibility of hydrogen embrittlement in pipeline steel a research gap.

Hydrogen atoms could reduce the toughness of metal and induce brittle fracture. Different metallurgical microstructures' hydrogen susceptibility differs greatly in steel, and no universal conclusion has been reached. Also, the hydrogen distribution is very difficult to test. Hence, no predictive model has been established to define HE susceptivity. According to previous research, several HE mechanisms have been proposed. Hydrogen-enhanced decohesion (HEDE) [4] indicates that

hydrogen atoms could reduce the bonding energy between adjacent iron atoms. As the cohesive force is reduced below the tensile force at the crack tip, the crack begins to propagate [5,6]. Most of the experimental and simulation results can support this theory. Based on the observation of the fracture surface and the dislocation slipping bands [7–10] under the fracture surface, some researchers proposed the hydrogen-enhanced local plasticity (HELP) theory. The HELP has clarified that hydrogen atoms could reduce the stacking fault energy and increase the density of dislocations [11–13]. The dislocation piling up can induce the increase of local stress, thus, enhancing the generation of microcracks [14]. Hydrogen atoms can also diffuse to the dislocation core. The dislocation movement would be hindered by hydrogen atoms. This phenomenon is named the hydrogen pinning effect [15]. Some other diffusible hydrogen atoms can be trapped by the phase interfaces, inclusion interfaces, and voids [16]. Those trapped hydrogen atoms can recombine into hydrogen gas. When the local hydrogen pressure exceeds the critical strength of the material, hydrogen-induced cracking occurs. This is the hydrogen bubble theory (HBT) [17,18].

The susceptibility of pipeline steel to HE is influenced by several factors, including the rate of hydrogen diffusion and the internal hydrogen concentration [19,20]. Previous research has demonstrated that external ambient temperature is crucial in determining the diffusion rate of hydrogen atoms and the internal hydrogen concentration of the

---

* Corresponding author at: College of Pipeline and Civil Engineering, China University of Petroleum (East China), Qingdao 266580, China.
** Corresponding author.
E-mail addresses: 20170079@upc.edu.cn (X. Xing), hao7@ualberta.ca (H. Zhang).
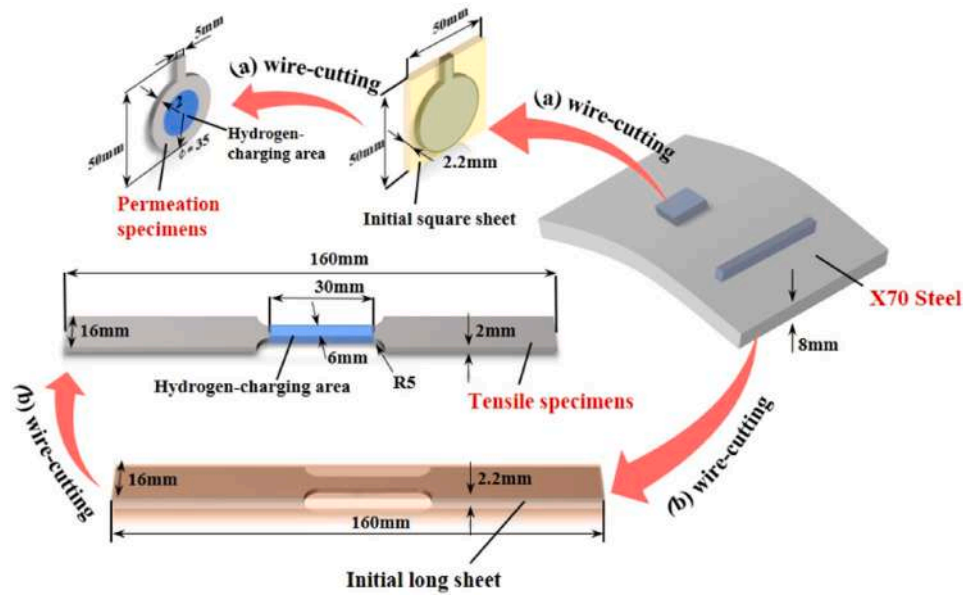
Fig. 1. Schematic diagram illustrating the processes for specimen manufacturing: (a) Devanathan-Stachurski test's specimen; (b) Standard tensile specimen.

Table 1
X70 chemical composition.

specimen	C/ %	Si/ %	Mn/ %	P/ %	S/ %	(V+Nb+Ti)/ %
X70	0.11	0.4	1.5	0.023	0.014	0.147

Table 2
X70 physical properties.

Grade	Yield strength/MPa	Tensile strength/MPa	Yield ratio
X70	533	572	0.932

material [21,22]. These findings suggest that temperature changes affect the HE susceptibility of X70 pipeline steel. Thus, it is necessary to clarify the influence of temperature on the diffusion and distribution of hydrogen atoms, as well as to quantify the atomic hydrogen concentration in steel at different temperatures. The diffusion of hydrogen atoms into steel involves a process of adsorption and desorption of hydrogen atoms on the steel surface. Zhang et al. [23] indicated that temperature changes affect the reaction parameters of both the adsorption and desorption processes. Specifically, an increment in temperature causes an increase in the number of transferred charges, leading to an increase in hydrogen atom concentration on the steel surface [24]. Also, the temperature increment could accelerate the combination of hydrogen atoms into molecules. Therefore, it facilitates the desorption of hydrogen molecules [25]. The hydrogen adsorption and desorption behaviors cause variations in the surface coverage of hydrogen atoms on the steel surface [26]. As a result, the hydrogen concentration adsorbed on the metal surface can become variable and difficult to quantify as temperature changes.

The temperature affects the atomic hydrogen concentration in the steel, and the increased atomic hydrogen concentration will change the fracture mode from ductile to brittle. The hydrogen-induced brittle fracture has been extensively studied about the crystallographic planes on which it occurs. Wang et al. [27] conducted a study examining the influence of crystal orientation on hydrogen diffusion and segregation in interstitial-free (IF) steels possessing BCC structure, revealing that hydrogen atoms preferentially accumulate at the {100} crystal plane, rendering these surfaces vulnerable to brittle cracking. Notably, when subjected to fatigue loading, the fatigue crack propagation is on the

{100} orientation [28,29]. Moreover, the {100} crystal plane is considered the dominant quasi-cleavage plane in BCC metals [30,31]. However, several studies have pointed out that in BCC metal structures, the plane where quasi-cleavage fracture often occurs is {110}, rather than {100} as aforementioned [32–35]. Particularly, F. Nakasato and Matsumoto investigated hydrogen-induced crack propagation in α-Fe through crystallographic studies and molecular dynamics simulations, respectively. Their findings proved that hydrogen on the {110} and {112} planes reduces the cohesive energy, significantly, which promotes crack propagation on both planes [36,37]. To date, no universal conclusion has been made on the preferable hydrogen-induced brittle fracture orientation. Also, the researchers have a debate on plastic deformation under the brittle plane. Previous research has demonstrated that the sliding of {112}<111> slip systems in BCC metals under static loading conditions is prone to twinning and slow toughness growth after sustained loading [38]. Ma [39] and Xing [40] employed molecular dynamics simulations to investigate the effect of hydrogen on BCC metal crack tips, revealing that the occurrence of brittle fracture at the crack tip, with {110}<111> slip systems being enhanced by hydrogen and the {110}<111> slip system is more prone to occur than the {112}<111> slip system. Even though several simulation results were conducted on the hydrogen-induced fracture plane orientation, no universal conclusion has been made. Also, there is a lack of experimental evidence of hydrogen-enhanced or inhibited plastic deformation.

In the current research, the D-S tests will be employed to test the diffusivity and concentration of hydrogen atoms at different temperatures. The SSRT tests are used to determine the temperature threshold of hydrogen embrittlement under different hydrogen charging currents in X70 steel. The underlying mechanism is illustrated, and a predictive model is established. Electron backscatter diffraction (EBSD) was used to probe the effect of hydrogen concentration on the orientation of brittle fracture surfaces. Also, the hydrogen effects on plastic deformation under the fracture plane and the primary slip system of dislocation are studied.

2. Experimental methodology

2.1. Preparation of specimen

The test specimens used in this work were machined from a sheet of X70 steel pipe with the thickness of 8 mm, as shown in Fig. 1. The
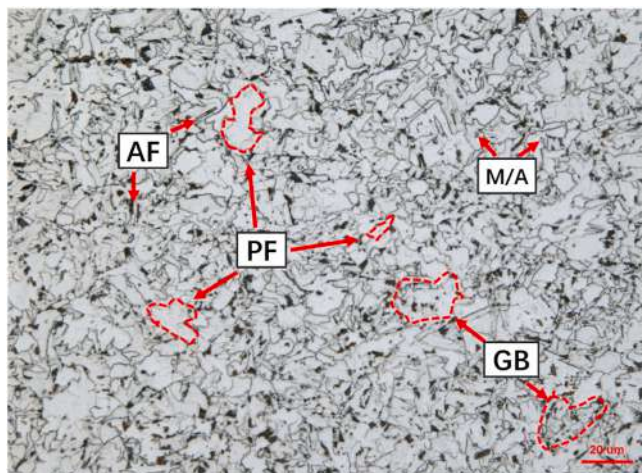
Fig. 2. The microstructure of X70 steel.

components of X70 steel are shown in Table 1. The tested physical properties in air are listed in Table 2. The X70 steel is polished using standard metallographic techniques and subsequently etched with 2 %

Nital solution for 5 s. As Fig. 2 has shown, the microstructure of the X70 is mainly composed of quasi-polygonal ferrite (PF), acicular ferrite (AF), M/A islands and granular bainite (GB). The processes for specimen-machining are shown in Fig. 1. In step (a), an initial square sheet of $50 \times 50 \times 2.2$ mm^3 was cut from X70 steel by wire cutting. The initial square sheet was then cut into a circular specimen with a diameter of 35 mm (20 mm in the hydrogen-charged area) and a thickness of 2 mm. In step (b), a sheet of $160 \times 16 \times 2.2$ mm^3 was cut from X70 steel by wire cutting. The initial long sheet was then cut into a standard tensile specimen. The thickness of the tensile specimen for slow strain tensile rate is 2 mm based on the standard GB/T 15970.7–2017, while the initial thickness of the sheet has a thickness of 2.2 mm. The specimen surface was ground by silicon carbide sandpapers with 400, 800, 1200, and 2000 grits. Subsequently, the specimens were degreased with acetone, and de-watered with anhydrous ethanol.

2.2. SSRT test

The experimental setup is shown in Fig. 3. The specimen is immersed in a solution of 0.5 mol/L H$_2$SO$_4$ and 0.1 g/L CH$_4$N$_2$S for hydrogen charging. All tests are carried out with the same loading rate of 0.0018 mm/min (1×10^{-6} s^{-1}). During the test, the unsealed sample is completely immersed in the hydrogen charging solution, and the

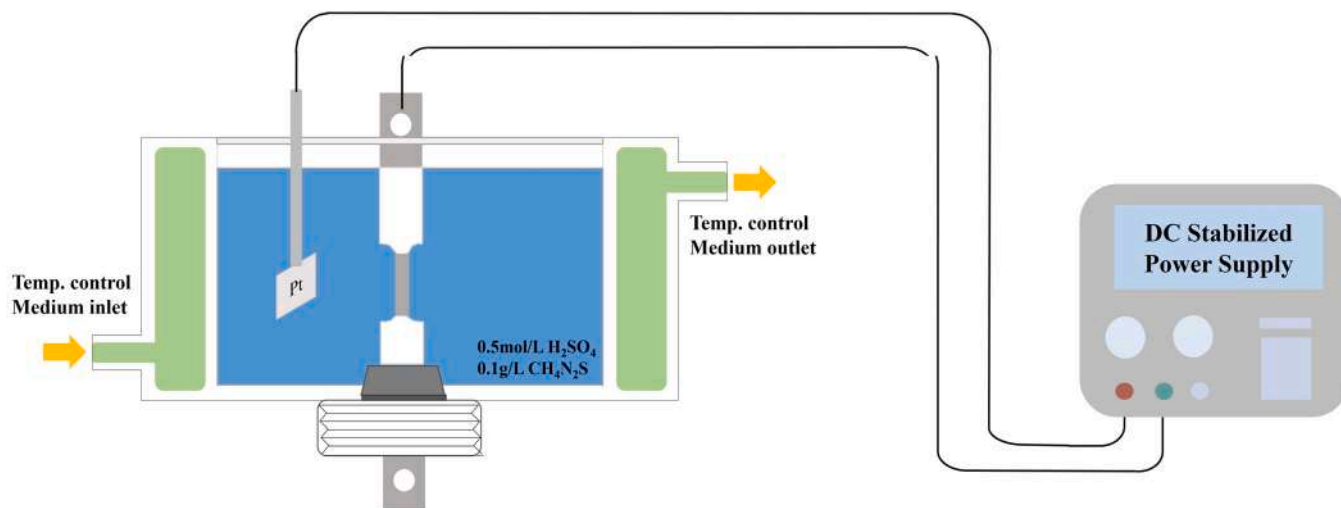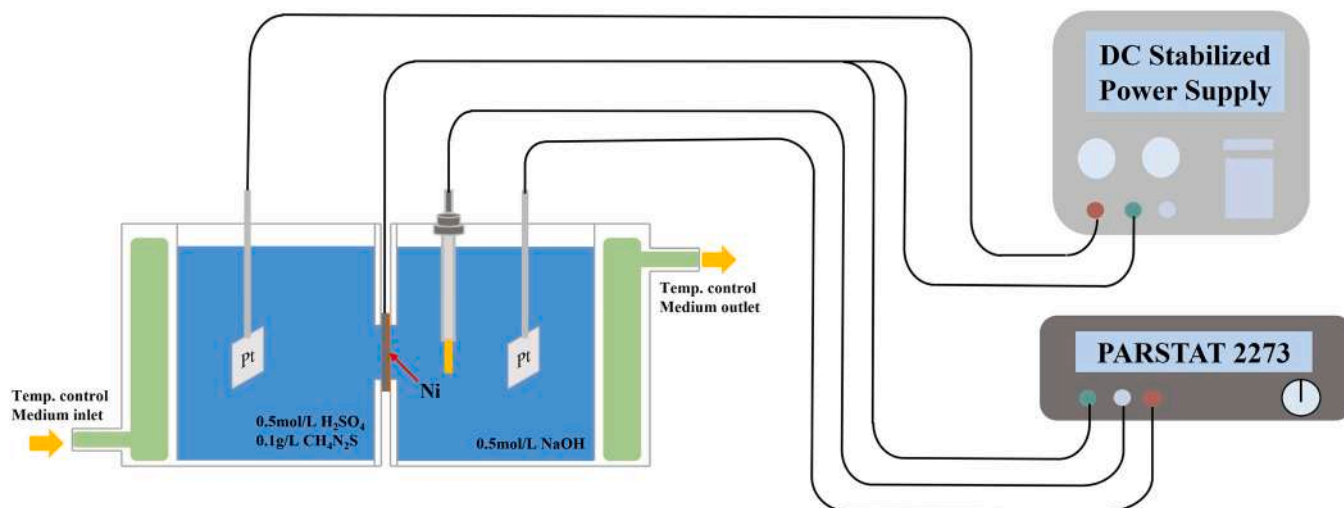**Fig. 3.** Schematic diagram of the experimental setup for slow strain rate tensile testing.

Fig. 4. Schematic diagram of the experimental setup for electrochemical hydrogen permeation test.
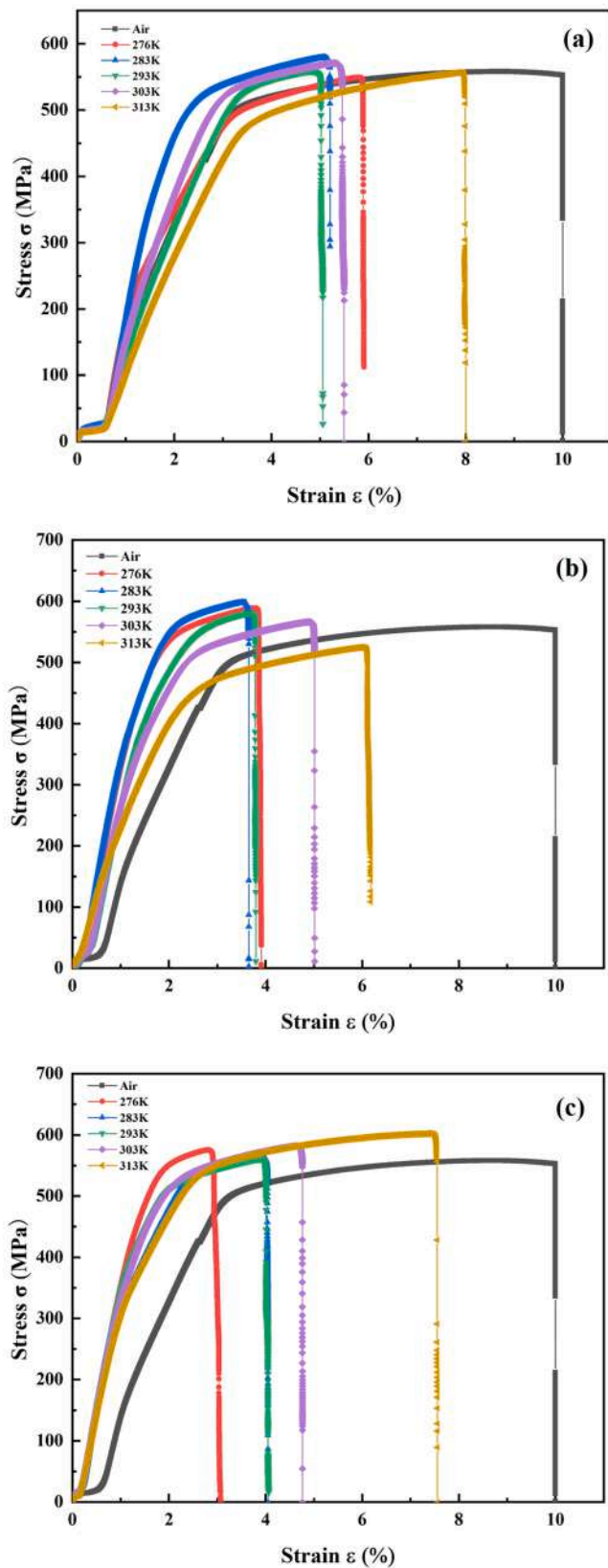
Fig. 5. The strain-stress curves of X70 steel under different charging currents : (a) 10 mA/cm^2; (b) 20 mA/cm^2; (c) 30 mA/cm^2.

temperature is controlled by a circulator. The SSRT experiments are conducted at temperatures ranging from 276 K to 313 K. Hydrogen atoms tend to be trapped at crystalline defects, such as vacancy, dislocations, surface, grain boundaries, phase boundaries, microvoids, and cracks, therefore, the local hydrogen concentration near the defect sites is much higher than the equilibrium hydrogen concentration typically measured experimentally. Some of the crystalline defects, such as vacancies, and dislocations, are multiplicated during the plastic deformation, which can further trap additional hydrogen when the tensile tests are conducted in a hydrogen environment. Hydrogen atoms can accumulate at defects, causing the formation of microcracks during the plastic deformation. Due to the hydrostatic stress field at the crack tip, a hydrogen-rich zone may form and cause crack propagation after a long-time accumulation in spite of the low current density [6,41]. Hence, our choice of a large current density is to accelerate the hydrogen-rich region formation process. Before the tensile test, the sample is pre-charged with hydrogen for 1 hour under the current of 10 mA/cm^2 to 30 mA/cm^2 to ensure saturation before stretching. The electrochemical hydrogen charging is maintained until the tensile specimen fractures. Meanwhile, comparative experiments are conducted under 293 K in the air.

2.3. Electrochemical hydrogen permeation test

Electrochemical hydrogen percolation experiments were conducted using a Devenathan-Stachurski (D-S) double electrolytic cell. An external DC power supply was used for electrochemical hydrogen charging in a solution containing 0.5 mol/L sulfuric acid (H$_2$SO$_4$) and 0.1 g/L thiourea (CH$_4$N$_2$S). An external PARSTAT2273 electrochemical workstation was used to oxidize the hydrogen atoms in a 0.5 mol/L solution of sodium hydroxide (NaOH). A three-electrode system was employed on the right side as an oxidation cell, with the nickel-plated side of the specimen as the working electrode, the platinum electrode as the auxiliary electrode, and the saturated glycerol electrode as a reference electrode. To investigate the effect of temperature, the D-S double electrolytic cell was designed with solution intercalation, as shown in Fig. 4, and controlled by a circulator. Before the experiment, a solution of sodium hydroxide (NaOH) with a concentration of 0.5 mol/L was purged with nitrogen (N$_2$) for 1 hour to eliminate oxygen from the solution.

2.4. Microstructural characterization

The fracture surfaces were carefully cut, degreased, dehydrated, and subsequently dried in a cold-air drying oven for 24 hours. To investigate the morphology of those sections, the specimens were purged with nitrogen gas and then subjected to SEM for observation. Subsequently, the fracture surfaces were mechanically ground and polished. Then, they were further polished with 10 % HClO$_4$ at a constant voltage of 20 V for 20 s. The ZEISS-SYMMETRY field emission gun is applied to the specimen. EBSD data were acquired at an accelerating voltage of 20 kV, emission current of 128.8 uA, tilt of 70°, and a scan step size of 0.25 μm on a hexagonal scan grid. Post-processing and data analysis were conducted using Channel 5 software.

3. Results

3.1. The Tensile test results

The strain-stress curves of X70 steel under different charging currents are shown in Fig. 5. The elongation at different temperatures can determine the HE susceptibility of the material. Moreover, the yield strength is the point where plastic formation starts to become predominant due to the motion of dislocations. An increase in the yield strength of a material indicates that plastic deformation has been inhibited. As the material is charged with hydrogen, the yield strength has a minor
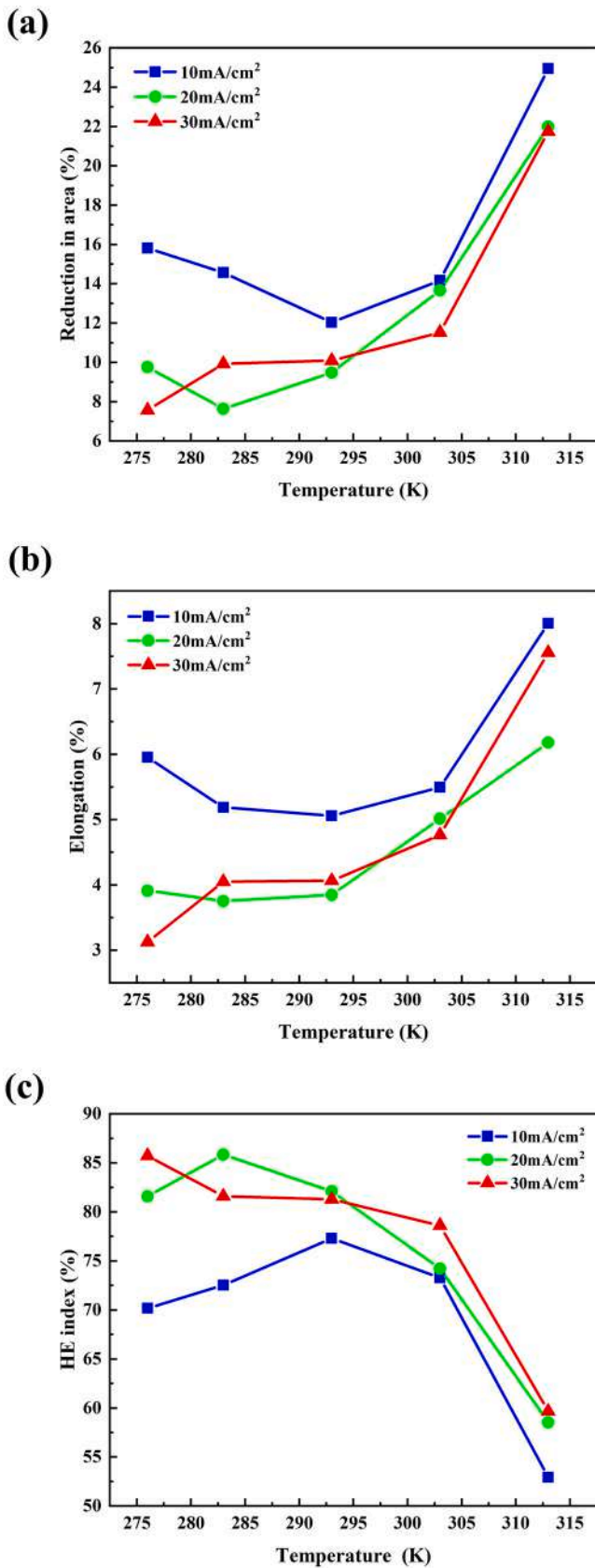
Fig. 6. The reduction in area, elongation, and HE index as a function of temperature at 10, 20, 30 mA/cm² current densities: (a) Reduction in area; (b) Elongation; (c) Hydrogen Embrittlement index.

increase, and the elongation has a significant decrease. Hence, the phenomenon indicates the occurrence of hydrogen-inhibited dislocation emission and hydrogen-induced toughness loss. Compared with the result in air, the elongation loss of samples with the hydrogen charging current of 10 mA/cm² is 40.94 %, 47.93 %, and 49.42 %, as the temperature increases from 276 K to 293 K. It indicates that the HE effect is enhanced as the temperature increases. However, as the temperature continually exceeds 293 K, the elongation of the X70 increases. The HE effect weakens with increasing temperature. Under 10 mA/cm² current, the HE is the most severe at 293 K. A similar pattern is also observed under 20 mA/cm² current. Compared with the result in the air, the samples endure 60.87 %, 63.47 %, 62.01 %, 49.85 %, and 38.23 % elongation loss as the temperature increases from 276 K to 313 K. The elongation loss attains a maximum of 283 K, which verifies that the HE effect is maximized. This temperature threshold disappears as the charging current is increased to 30 mA/cm². As the temperature increases from 276 to 313 K, the elongation loss is 69.14 %, 59.52 %, 59.34 %, 52.36 %, and 24.46 % compared with the result in the air. The ductility of the specimen increases with the temperature. Apparently, X70 steel exhibited notable toughness recovery at 313 K at a current density of 30 mA/cm². The increase in temperature always enhances the desorption rate of hydrogen atoms [24]. It is expected that the adsorption rate at the charging current density of 30 mA/cm² reaches a maximum rate, even at low temperatures, hence, the increase in temperature will not affect the adsorption rate at this high charging current density, but only enhance the desorption rate, causing a decrease in the equilibrium hydrogen concentration with temperature on the surface. At the charging density of 20 mA/cm², the adsorption rate does not reach the maximum at the lowest temperature in the current study but would increase with temperature and reach the maximum at the intermediate temperature. Finally, both the adsorption rates of hydrogen at 30 and 20 mA/cm² at 313 K have reached maximum. And the desorption rates of hydrogen at these two current densities are identical. Thus, the hydrogen concentrations at these two currents are similar at 313 K. This postulation has been verified in Fig. 14(a), and a detailed description can be found in Section 4.1. Hence, the specimens should have similar elongations at 313 K and at 20 and 30 mA/cm² current densities. However, the exact reason why the elongation under the highest applied current density is higher than that of 20 mA/cm² at 313 K is still unknown, and this phenomenon clearly requires further investigation.

The reduction in area ψ, the elongation δ, and the hydrogen embrittlement index are calculated and shown in Fig. 6. The formulas can be expressed as follows:

$$\psi = \frac{A_0 - A_f}{A_0} \times 100 \tag{1}$$

$$\delta = \frac{L_f - L_0}{L_0} \times 100\# \tag{2}$$

$$HE \quad index = \frac{RoA_{air} - RoA_{HC}}{RoA_{air}} \times 100 \tag{3}$$

where A_0 is the original loading area (mm²), A_f is the fracture surface area (mm²), L_0 is the original length of the specimen (mm), and L_f is the specimen length after fracture (mm), the RoA_{air} and RoA_{HC} are the reduction of area after SSRT in the in-air and hydrogen-charged (HC) conditions. The ψ and δ values follow the same tendency. As the charging current is 10 mA/cm², the ψ and δ values approximate minimums at 293 K. In addition, we conducted Charpy impact tests to compare with the results in SSRT tests under 10 mA/cm². Fig. S1 in Supplementary Information (SI) clearly shows that the impact energy reaches a minimum at 293 K, which exhibits the trend of SSRT tests. While the charging current is 20 mA/cm², the ψ and δ values reach minimums at 283 K. Those minimum values indicate the most severe HE susceptibility. However, as the charging current increases to 30 mA/cm², ψ and δ values increase with temperature, which verifies the
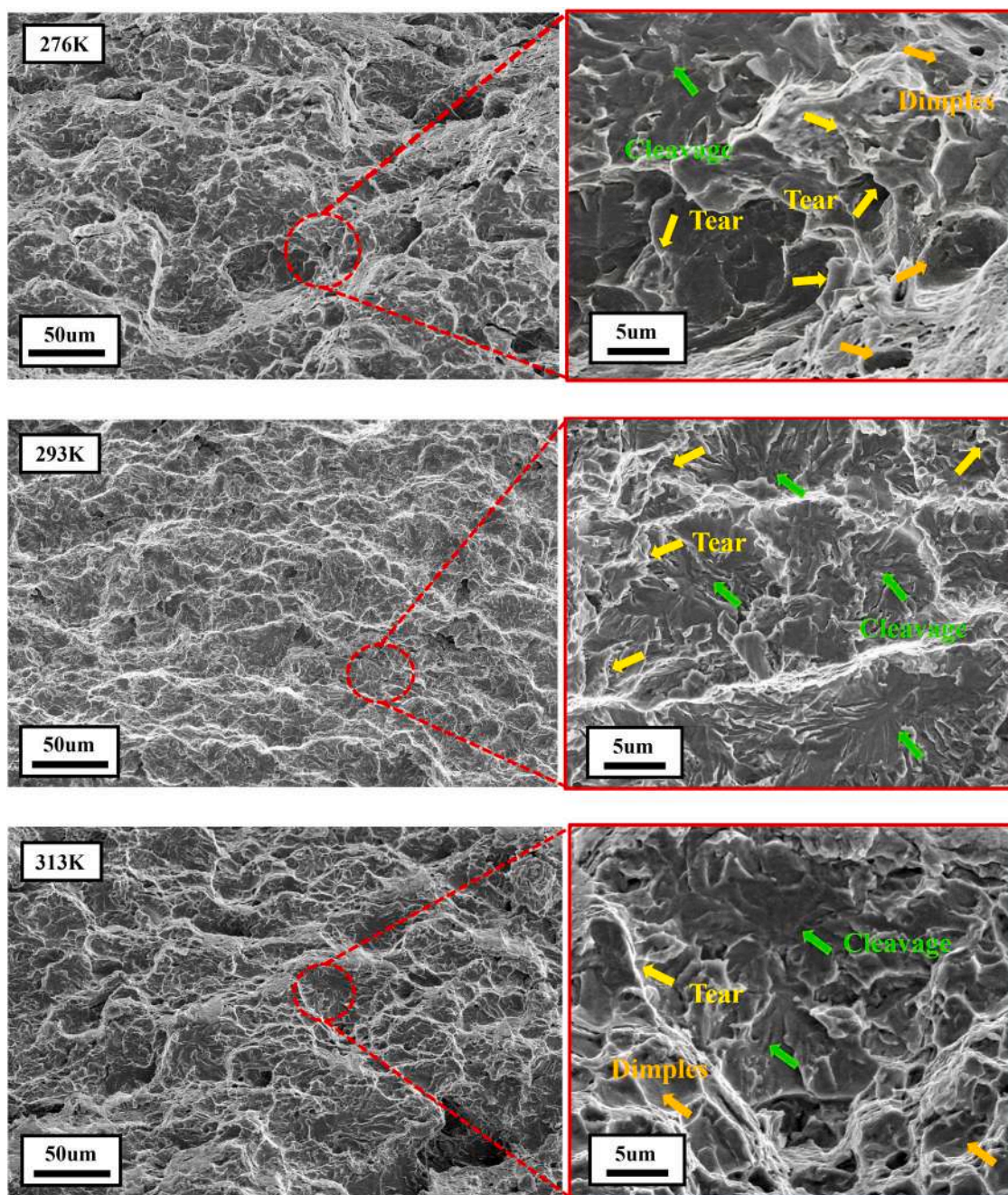
Fig. 7. SEM images of fracture surface in X70 steel under 10 mA/cm^2 at the temperature of 276 K, 293 K and 313 K.

ductility increases with temperature. The HE index illustrates the HE susceptibility. The peak of the HE index indicates the most severe HE occurrence. The peak values are detected at 293 and 283 K, as the charging current densities are 10 and 20 mA/cm^2, respectively. The HE index decreases with the temperature at 30 mA/cm^2. All these outcomes verify the existence of a critical temperature to maximize the HE at moderate charging current densities. The critical temperature disappears as the charging current density increases to a large value (30 mA/cm^2).

The SEM images of fracture areas under different temperatures and charging currents are shown in Fig. 7 (10 mA/cm^2), Fig. 8 (20 mA/cm^2), and Fig. 9 (30 mA/cm^2). The SEM images of the fracture surface at the lowest and highest temperatures are selected. In addition, the SEM images of temperatures at which the most severe HE occurs under 10 and 20 mA/cm^2 are also displayed. At a hydrogen charging current of

10 mA/cm^2, the dimples' number and size become smaller below 293 K but increase above 293 K. Furthermore, distinct river-like cleavage patterns and tearing patterns are observed in the morphology of the cross-section at 293 K. This phenomenon indicates that the HE susceptibility is maximized at a charging current of 10 mA/cm^2 and $T = 293$ K. At charging currents of 20 mA/cm^2, the brittle fracture SEM image with the most cracking platform is indicated under 283 K. At the charging current of 30 mA/cm^2, the cleavage area decreases, and the number of dimples increases with the temperature increment. The Digimizer software is employed to measure the total proportion of the dissociated surface area within a designated region of 417.3 μm × 273.4 μm at the center of the fracture surface, as shown in Fig. 10. It verifies the existence of temperature thresholds at charging currents 10 mA/cm^2 and 20 mA/cm^2. Moreover, we also detect that the percentages of cleavage areas at 20 mA/cm^2 and 30 mA/cm^2 are similar but they are
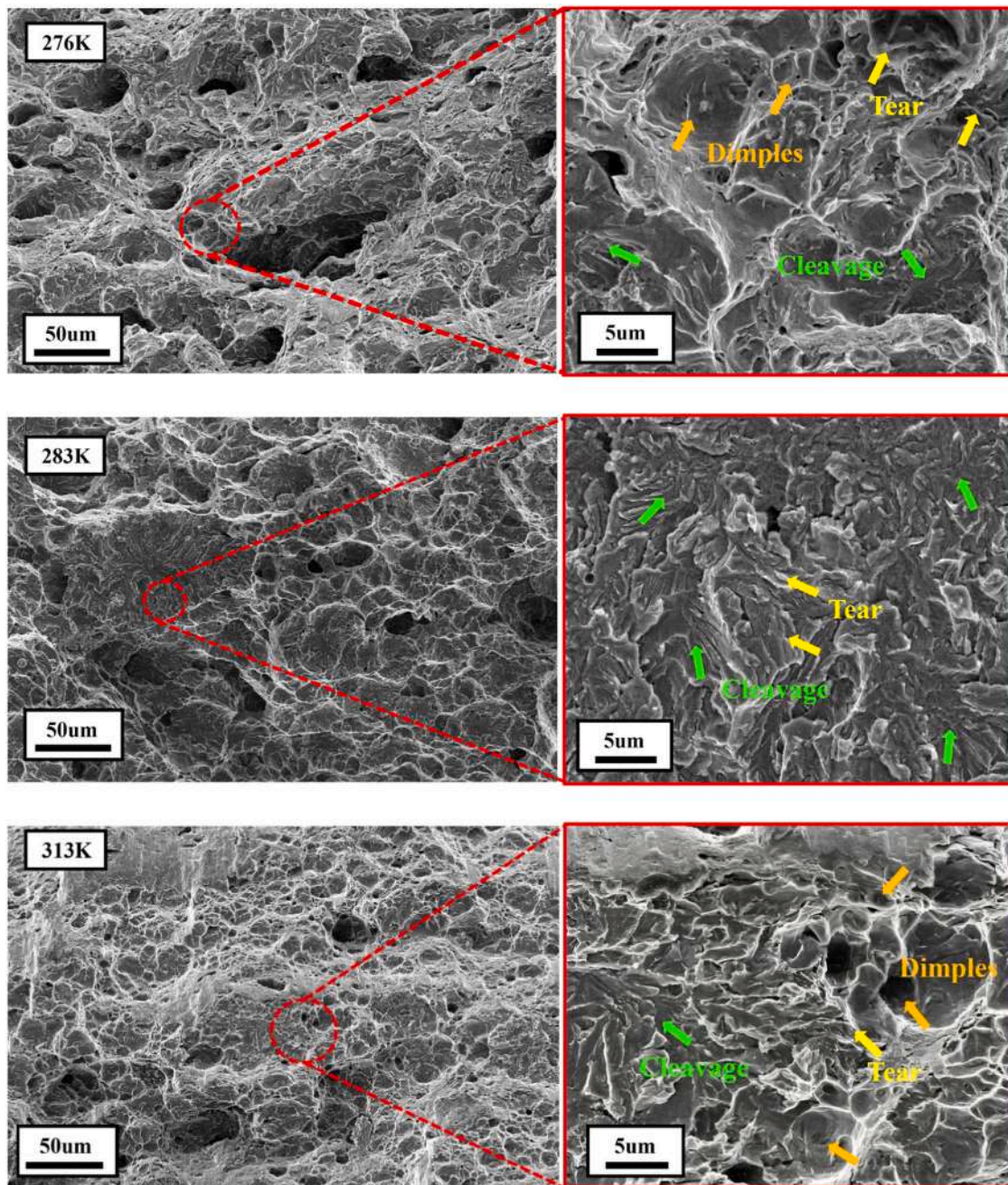
Fig. 8. SEM images of fracture surface in X70 steel under 20 mA/cm^2 current at the temperature of 276 K, 283 K and 313 K.

substantially larger than that at 10 mA/cm^2. The hydrogen susceptibility becomes severe with the increase of the charging current at 276 K. The adsorption rates of hydrogen on the specimen surface increase with temperature and reach maximums at intermediate temperatures of 10 and 20 mA/cm^2 current densities. Thus, the brittle area percentage increases below an intermediate temperature of above current densities. The hydrogen adsorption rate reaches the maximum at 30 mA/cm^2 of 276 K in current tests, and the hydrogen concentration is only affected by desorption rate enhancement of temperature increment. Consequently, the percentage of cleavage plane decreases with temperature at 30 mA/cm^2. This phenomenon is verified in Fig. 14(a), which shows the variation of apparent hydrogen equilibrium concentrations under different temperatures and charging currents.

3.2. The hydrogen permeation test

To analyze the temperature effect on HE, the hydrogen diffusion and segregation should be studied. Hence, we conducted the D-S tests to study the diffusion and equilibrium concentration of hydrogen under different temperatures.

The detected current density versus time has been shown in Fig. 11. All curves have two platform periods, where curves parallel to the x-axis. The length of the first parallel part for each curve indicates the time first detecting the hydrogen permeation current. It is the time for hydrogen atoms to permeate the specimen. The height of the second parallel part indicates the stabilized current density, which is related to the equilibrium hydrogen flux. Both factors determine the equilibrium hydrogen concentration in the specimen. In Fig. 12, it is evident that the steady-state hydrogen percolation current density exhibits a linear increase as
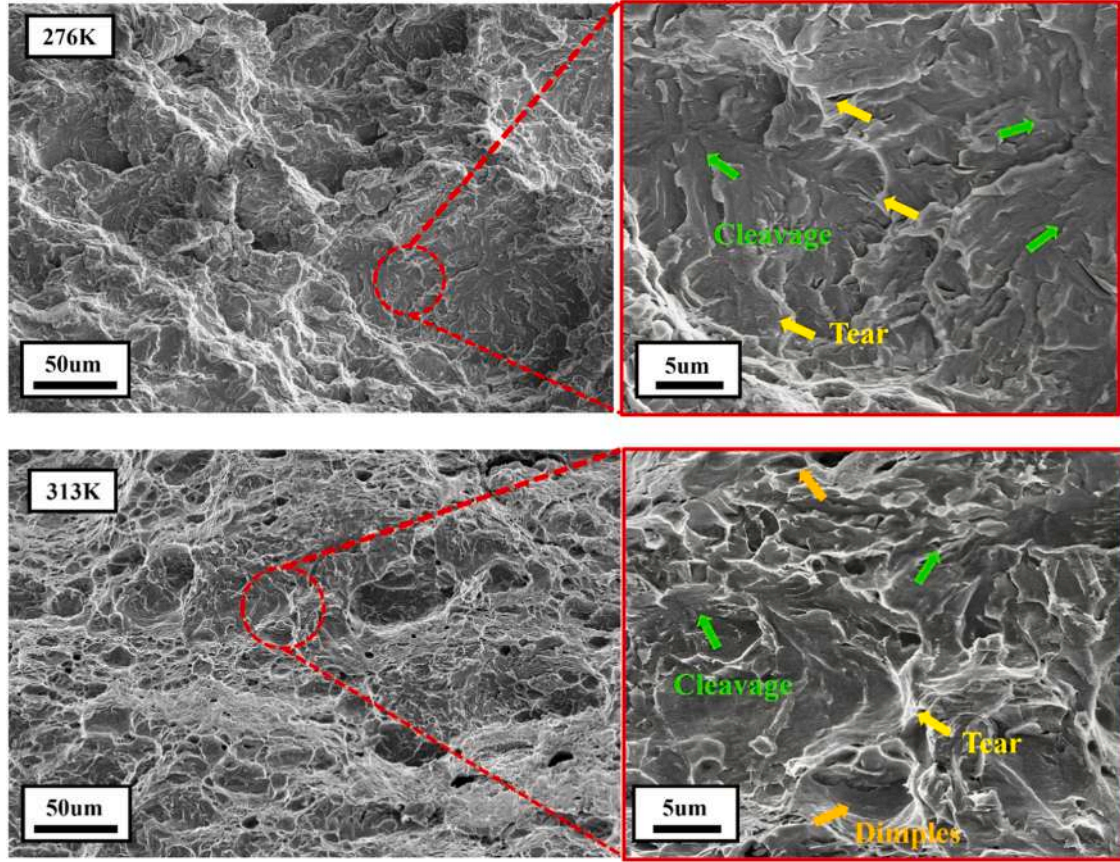
Fig. 9. SEM images of fracture surface in X70 steel under 30 mA/cm^2 at the temperature of 276 K and 313 K.
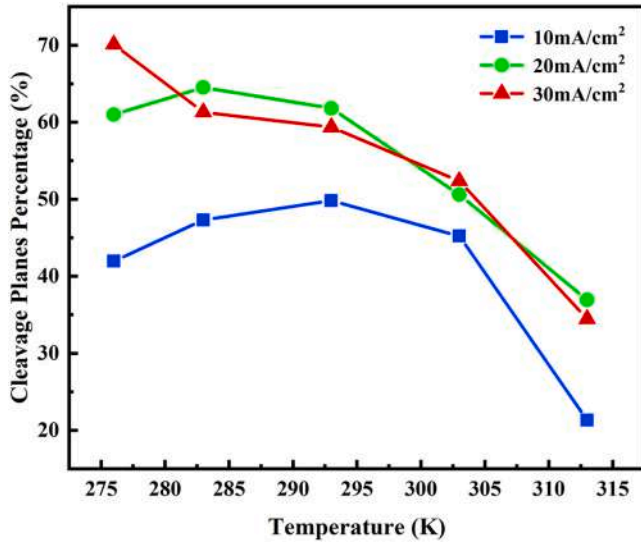

Fig. 10. Under the three hydrogen-charging current densities, the proportion of cleavage area changes with temperature.

a function of temperature.

We could calculate the equilibrium hydrogen concentration with permeation time and stabilized permeation current by the constant concentration (CC) and constant flux (CF) models. The CC and CF models have been expressed as [42,43]:

$$\text{CC model}: \frac{I_t}{I_\infty} = \frac{2}{\sqrt{\pi\tau}}\sum_{n=0}^{\infty}\exp\left(-\frac{(2n+1)^2}{4\tau}\right) \tag{4}$$

$$\text{CF model}: \frac{I_t}{I_\infty} = 1 - \frac{4}{\pi}\sum_{n=0}^{\infty}\frac{(-1)^n}{(2n+1)}\exp\left(-\frac{(2n+1)^2\pi^2\tau}{4\tau}\right) \tag{5}$$

Where I_t is the permeation current at instant time t, I_∞ is the steady state value of the hydrogen permeation current, n is a dimensionless constant, the time τ is equal to Dt/L^2, in which D is the hydrogen diffusivity (cm^2/s), and L is the thickness of the specimen (mm).

The comparison of the CC and CF models with experimental results is shown in Fig. 13. The CC models matches better with experimental tests under all temperatures. Hence, we apply the CC model to calculate the diffusivity (D_{eff}) and surface equilibrium concentration of hydrogen (C_0). The expressions are shown as below:

$$D_{eff} = \frac{L^2}{6t_L} \tag{6}$$

$$C_0 = \frac{J_\infty L M_H}{\rho_{Fe} D_{eff} F} \times 10^6 \tag{7}$$

where t_L is the time required as $I_t = 0.63I_\infty$, M_H is the molar density of hydrogen (1 g/mol), ρ_{Fe} is the density of iron (7.87 g/cm^3), J_∞ is the steady-state hydrogen permeation flux (mol/cm^2/s).

Fig. 14 shows the surface hydrogen concentration (C_0) and hydrogen diffusion coefficient variation as a function of temperature. The hydrogen diffusivity is enhanced by temperature. Fig. 14(a) shows that the hydrogen concentration at 30 mA/cm^2 monotonically decreases with temperature, while the equilibrium concentration at 10 mA/cm^2 and 20 mA/cm^2 both show a peak at the intermediate temperature, and
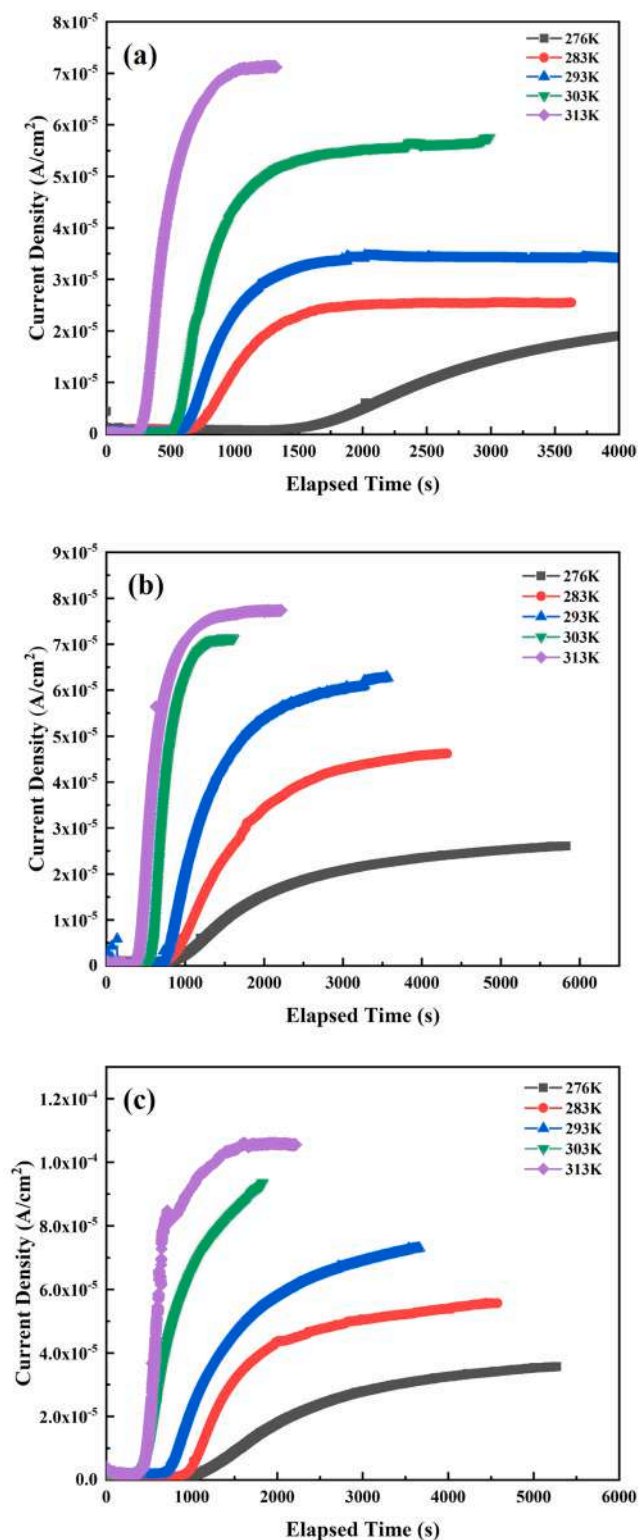
Fig. 12. Variation of steady-state hydrogen percolation current density with temperature at 10 mA/cm^2, 20 mA/cm^2, and 30 mA/cm^2 currents.

demonstrate that the HE susceptibility of the X70 steel under different temperatures could be predicted with the C_0 value calculated from the CC model. In Fig. 14(b), the hydrogen diffusion coefficient is increased by current density. In a perfect crystal, the hydrogen diffusion coefficient should not depend on the applied current. In Fig. 15, we show the Arrhenius plot of the calculated effective diffusion coefficients at different charging current densities, i.e., ln$D$ and 1/T. Apparently, the diffusivity follows the Arrhenius relationship, i.e., $D = D_0 \exp(-Q/k_B T)$, where Q is the activation enthalpy, which can be obtained by the slope of the curve. With no surprise, the slopes for different charging current densities are almost identical, suggesting the diffusion mechanisms do not change when the current density varies from 10 mA/cm^2 to 30 mA/cm^2. However, the diffusion of lattice hydrogen in real materials is highly impacted by its interaction with hydrogen trapping sites [44,45]. As indicated by Fick's first law, under the steady-state diffusion condition, the hydrogen flux is positively related to the hydrogen diffusivity and hydrogen gradient. Generally speaking, at each temperature, the hydrogen concentration on the charging side increases with current density (see Fig. 14(a)). Hence, the hydrogen flux increases with the increase of current densities. However, the difference in hydrogen concentration between different current densities becomes smaller as temperature goes higher, due to the competition between adsorption and desorption with temperature. In a recent study of the determination of hydrogen bulk diffusion in three industrial produced dual phase steels, Drexler et al. suggested that the effective hydrogen diffusion depends both on the lattice hydrogen concentration and hydrogen trapping densities [46]. In the current study, since the trapping site densities are constant throughout the sample and they are all expected to be filled at the end of charging, the number of trapping hydrogen atoms remains constant although the charging current increases. However, the increase of current density would inevitably increase the hydrogen flux, i.e., the total number of hydrogen atoms, making the percentage of lattice hydrogen increase, in which the lattice hydrogen atoms have a much higher diffusivity than trapped hydrogen atoms [47]. In addition, Namboodhiri and Nanis also pointed out that the hydrogen diffusivity in Armco iron depends on the local hydrogen concentration, and it increases with the concentration [48]. Therefore, it is reasonable to expect the effective hydrogen diffusion coefficients will increase with charging current density.

Fig. 11. The D-S tests under different temperatures and charging currents: (a) 10 mA/cm^2; (b) 20 mA/cm^2; (c) 30 mA/cm^2.

this temperature tends to be higher at lower charging current density. This trend approximates the change in hydrogen embrittlement susceptibility to temperature. Also, the C_0 maximums are verified at 293 K and 283 K, as charging currents are 10 mA/cm^2 and 20 mA/cm^2, respectively. The C_0 value is diminished with a temperature under 30 mA/cm^2, as the hydrogen embrittlement susceptibility is also weakened by the temperature at this charging current. These outcomes
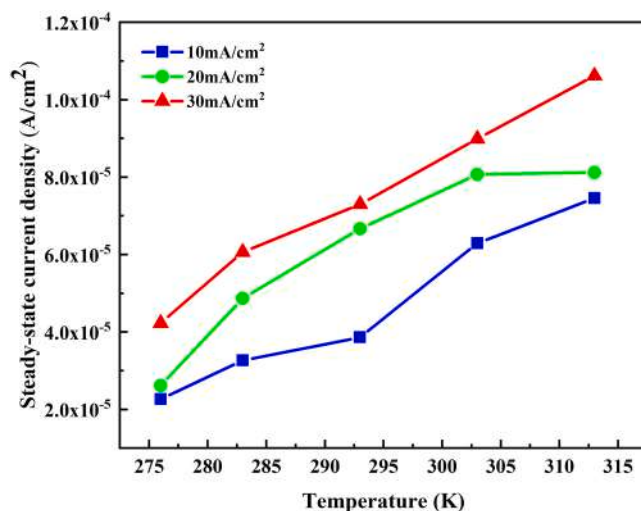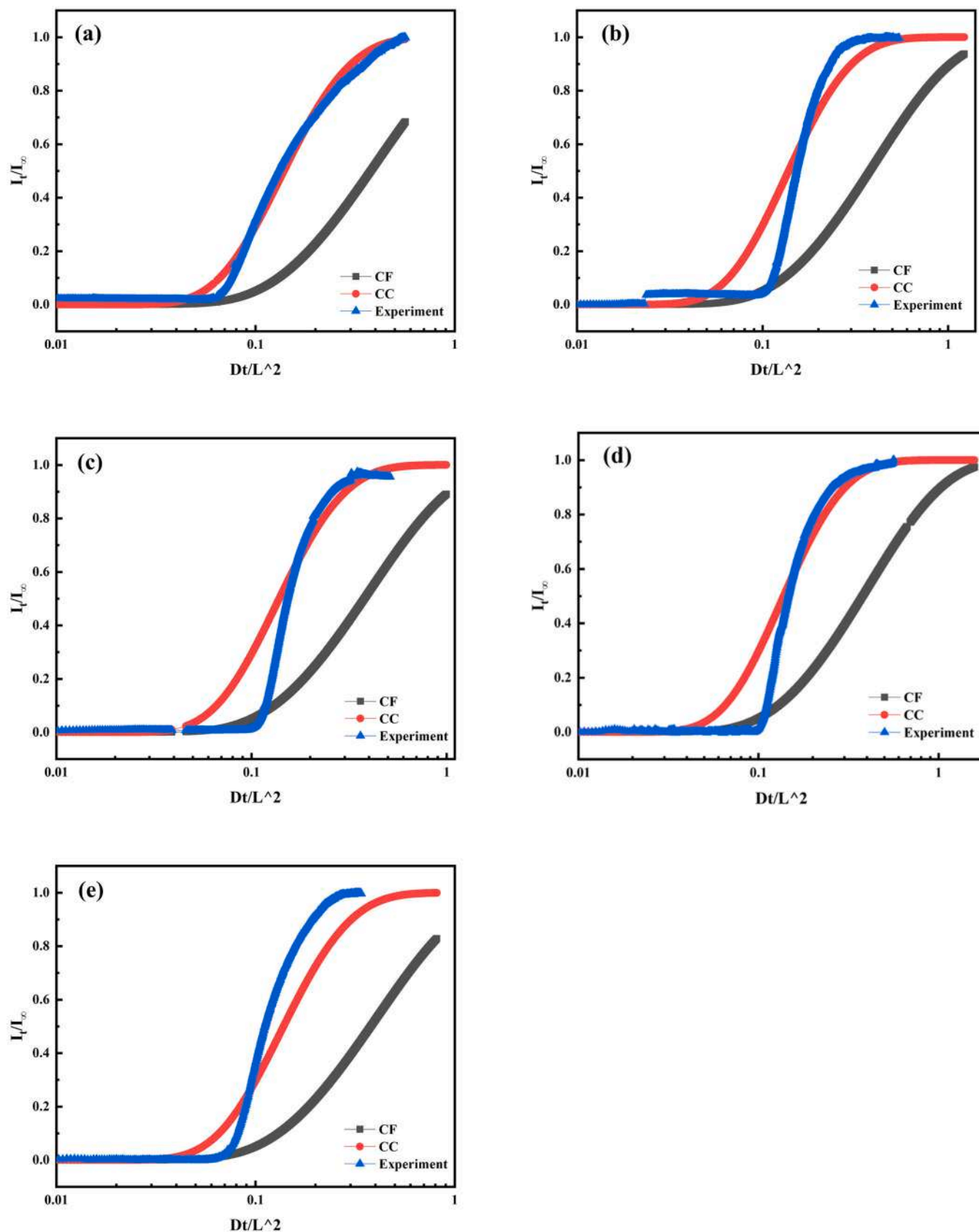
Fig. 13. The comparison of CC and CF models with experimental results under 10 mA/cm^2, (a)-(e) indicate 276 K, 283 K, 293 K, 303 K, and 313 K.
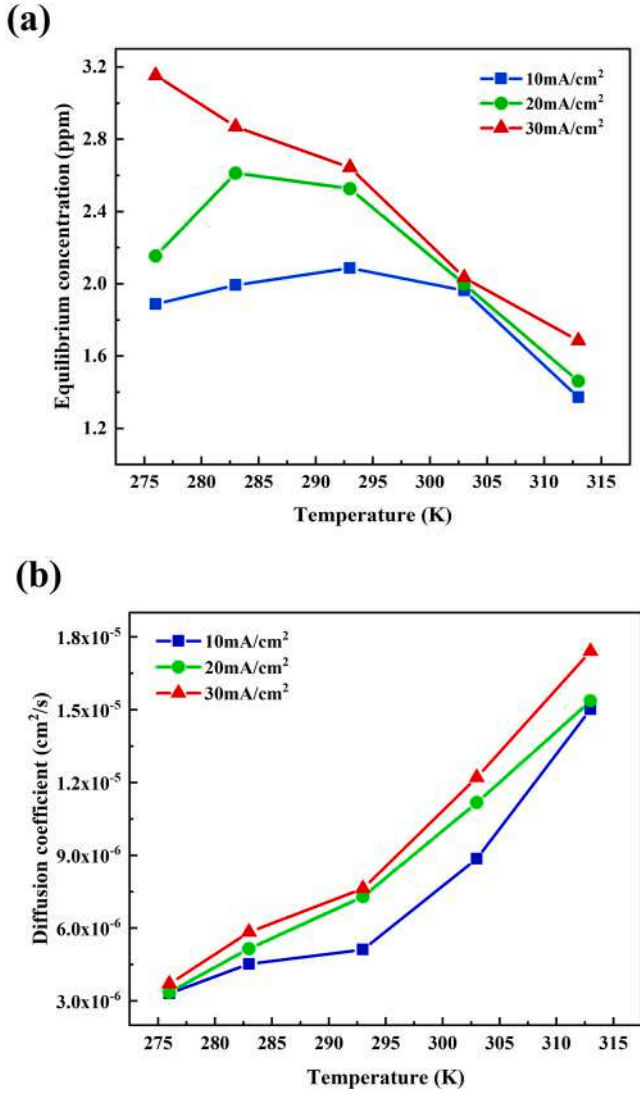
Fig. 14. The equilibrium concentration and hydrogen diffusion coefficient of X70 steel specimens as a function of temperature: (a) Equilibrium concentration at three current densities of 10, 20 and 30 mA/cm²; (b) Diffusion coefficient at three current densities.
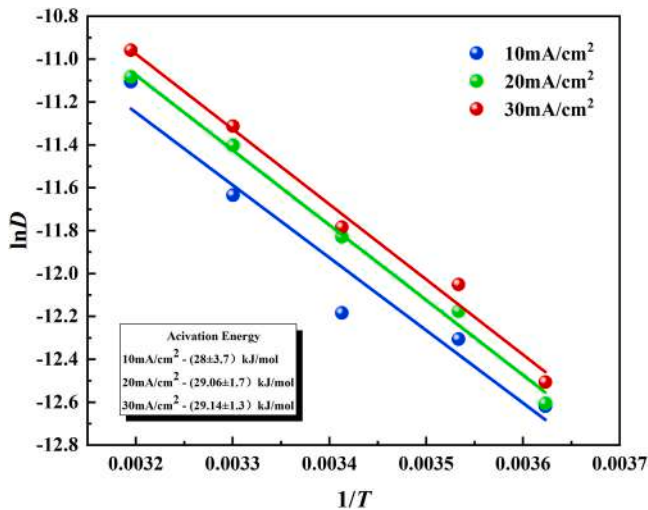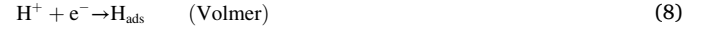

Fig. 15. The plot of ln D as a function of $1/T$ at different charging densities.

4. Discussion

4.1. The temperature dependence of hydrogen evolution reaction (HER)

Three reaction functions can be applied to illustrate the hydrogen generation and adsorption processes, as shown in Eqs. (8)–(10). These three functions are named Volmer-Tafel-Heyrovsky mechanisms.

$$H^+ + e^- \rightarrow H_{ads} \qquad (Volmer) \tag{8}$$

$$H_{ads} + H_{ads} \rightarrow H_2 \quad (Tafel) \tag{9}$$

$$H_{ads} + H^+ + e^- \rightarrow H_2 (Heyrovsky) \tag{10}$$

As temperature increases, the kinetic energy of hydrogen atom is enhanced. The Arrhenius formula can predict the change of active hydrogen in Volmer reaction. The equation is shown as:

$$k_{ads} = A\exp\left(\frac{-E_{ads}}{RT}\right) \tag{11}$$

Where k_{ads} is the parameter quantifying the velocity of the adsorption process, A is the pre-exponential factor, which is between 0 and 1, representing the combination ratio of the H_{ads} into H_2, R is the gas constant, T is the temperature, and E_{ads} is the minimum activation energy required for the reaction. As temperature T increases, the value of k_{ads} increases correspondingly, which indicates that the number of adsorption hydrogen atoms H_{ads} increases. Thus, the Volmer reaction could enhance hydrogen embrittlement in steel. If the coverage of hydrogen atoms on the steel surface is moderate, the Heyrovsky reaction is in function. The H_{ads} and H^+ can combine into H_2. Under a large coverage of hydrogen atoms, the Tafel reaction is dominant, that two H_{ads} combine into H_2. These two desorption reactions can hinder hydrogen embrittlement by releasing hydrogen gas. The Tafel slope could be used to illustrate the velocity of the Heyrovsky and Tafel reaction, and the expression is shown below [49] :

$$b = -\frac{2.303RT}{\alpha F} \tag{12}$$

Where α is a constant, and F is the Faraday constant. The Tafel reaction is also facilitated by temperature. The smaller the Tafel slope, the better the reactivity. Namely, the desorption reaction rate also increases with increasing temperature [50,51]. Generally speaking, both the adsorption rate (the number of hydrogen atoms adsorbed on the surface per unit time) and desorption rate (the number of hydrogen atoms left on the surface per unit time) increase with temperature. Based on the equilibrium hydrogen concentration results shown in Fig. 14(a), we postulate that the equilibrium concentration on the surface is a result of the competition between hydrogen adsorption rate and desorption rate with temperature. Typically, the hydrogen embrittlement is influenced by hydrogen diffusion and accumulation in the metal [40,41]. The atomic hydrogen concentration on the specimen surface determines the amount of hydrogen that enters the specimen. Also, we prove that the HE sensitivity is directly related to the atomic hydrogen concentration on the surface calculated from the CC model in Section 3.2. The ratio of the Arrhenius formula and Tafel slop can characterize the hydrogen atom coverage on the specimen [52]. Hence, it's reasonable to characterize the susceptibility of HE in steel by the ratio (η) of the Arrhenius formula and the Tafel slope. The expression is shown as:

$$\eta = -\frac{A\exp(\frac{-E_{ads}}{RT}) \times \alpha F}{2.303RT} = B\frac{\exp(\frac{-E_{ads}}{RT})}{T} \tag{13}$$

Where $B = -\frac{A\alpha F}{2.303R}$ is defined as an environmental factor. If we make a derivation of η with T, the η' could be shown as:
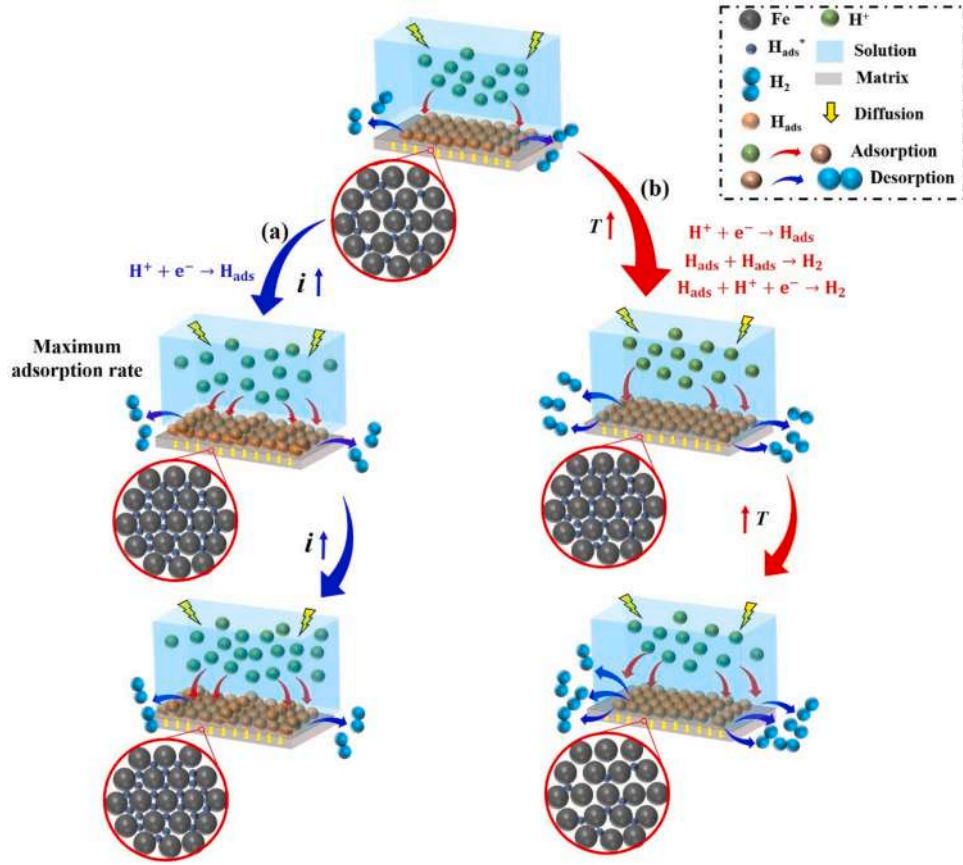
Fig. 16. Schematic illustration of the adsorption and desorption of hydrogen atoms on the surface of specimen as affected by (a) increasing current density at a constant temperature; and (b) increasing temperature at a constant current density.
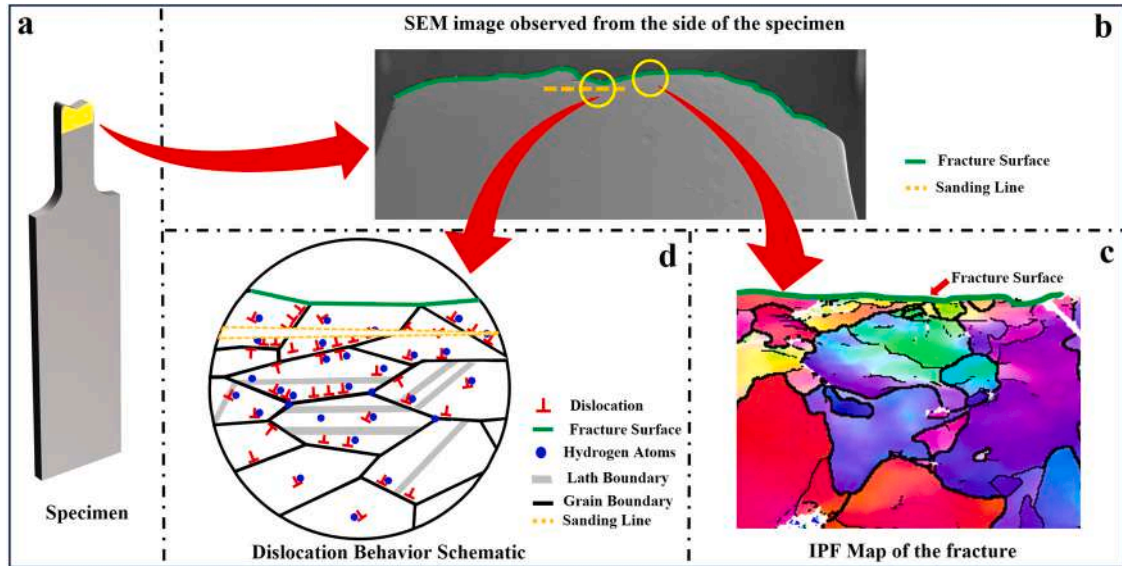

Fig. 17. Schematic diagram of the observing area in EBSD tests.

$$\eta^{'} = B\frac{\exp\left(\dfrac{-E_{ads}}{RT}\right)\left[\dfrac{E_{ads}}{RT} - 1\right]}{T^2} \tag{14}$$

Defining the temperature at which $\eta^{'} = 0$ as the critical temperature $T_{critical}$, the value of it should be E_{ads}/R. If $\eta^{'} > 0$, which indicates $T < T_{critical}$, the η will increase with temperature. It is verified that the HE

susceptibility of steel increases with temperature as the temperature below $T_{critical}$. And when $\eta^{'} < 0$, which indicates $T > T_{critical}$, the η will decrease with temperature. It's demonstrated that the HE susceptibility is weakened by temperature as the temperature above $T_{critical}$. Notably, E_{ads} is generally related to the state of the specimen surface and is mainly affected by the degree of hydrogen atom coverage on the steel. The adsorption energy is more negative as the coverage of hydrogen
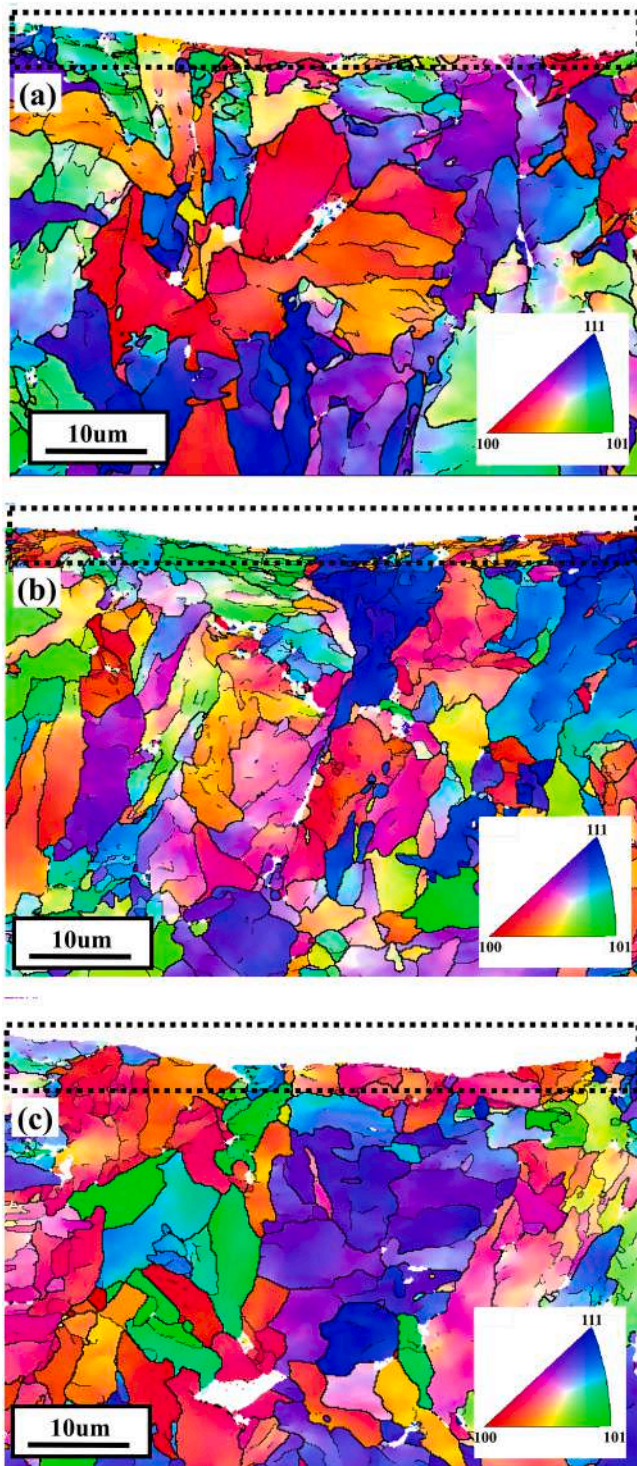
Fig. 18. Inverse pole figure (IPF) maps: (a) hydrogen charging current density of 20 mA/cm^2 at 276 K; (b) hydrogen charging current density of 20 mA/cm^2 at 283 K; (c) hydrogen charging current density of 20 mA/cm^2 at 313 K.

increases, namely, the charging current increases [53]. Hence, the $T_{critical}$ value would drop as the charging current increases. This tendency matches well with current experimental tests. Also, the temperature change has little effect on the adsorption energy of hydrogen on the iron surface, and it was shown that the adsorption energy changed by 0.01 eV when it was increased from 100 K to 300 K [54]. Thus, the $T_{critical}$ is mainly dependent on the concentration of hydrogen on the steel.

The above calculation proves the existence of a critical temperature that maximizes the HE in steel. It also indicates that the hydrogen concentration on the steel surface reaches a maximum at the critical temperature. However, the critical temperatures are only verified in low hydrogen concentrations, where the coverage of hydrogen atoms on the metal surface is limited. The temperature effects on hydrogen desorption and adsorption on steel surface under different current densities are shown in Fig. 16. As charging currents equal to 10 and 20 mA/cm^2, the adsorption rate of hydrogen on the specimen surface is moderate at 276 K. Increasing the charging current will increase the hydrogen atoms absorbed on the specimen. However, if the adsorption rate of the hydrogen atom reaches the maximum, the further increase of current density will not increase the hydrogen atom adsorption, as shown in Fig. 16(a). At the highest charging current density, i.e., 30 mA/cm^2, the adsorption rate reaches maximum even at the lowest temperature, hence, the adsorption rate remains constant for the entire temperature range. Since the desorption rate increases with temperature, the overall rate of keeping hydrogen atoms on the surface, i.e., the equilibrium concentration would monotonically decrease with temperature. At the charging density of 20 mA/cm^2, the adsorption rate does not reach the maximum at the lowest temperature in the current study but would increase with temperature and reach the maximum at the intermediate temperature. The initial increase in adsorption rate with temperature exceeds the increase in desorption rate with temperature, causing the equilibrium hydrogen concentration to increase with temperature [24], but the increase in adsorption rate with temperature slows down and reaches the maximum at the intermediate temperature, resulting in the decrease in the equilibrium concentration at higher temperatures, as shown in Fig. 16(b). A similar process would occur to the lowest charging current density, i.e., 10 mA/cm^2, except the maximum adsorption rate would be reached at an even higher temperature, resulting in the shift of the peaking of equilibrium hydrogen concentration to a higher temperature.

4.2. The hydrogen effect on plastic behavior and fracture surface's orientation

EBSD characterization is performed to investigate the effect of hydrogen on plastic behavior and grain orientation in brittle fractures. Aiming to reveal the crystallographic orientation of the fracture surface, we conducted the polishing and EBSD tests in the normal direction to the sheet-type tensile specimen to detect the fracture surface orientation from a side view, shown as the green line in Fig. 17(c). The green line represents the contour of the fracture surface. When observing the hydrogen effect on dislocation emission, we do not have to detect the dislocation behavior on the fracture surface. The hydrogen atoms and dislocations are prone to accumulate at the regions where large deformation or tensile stress is presented. The region near the fracture plane usually suffers a large strain under tensile test conditions. More hydrogen atoms would diffuse to, and more dislocations could be generated near the fracture surface during the tensile test [55]. Thus, the plane beneath the fracture surface could be selected to illustrate the hydrogen effect on dislocation generation, as Fig. 17(d) shows.

The hydrogen-affected fracture surfaces with maximum (276 K) and minimum (313 K) temperatures, and the specimen with the most HE susceptibility (283 K) at the charging current density of 20 mA/cm^2 are characterized using EBSD. Characterization of the fracture plane orientations is typically accomplished using an inverse pole figure (IPF) diagram, as depicted in Fig. 18. The fracture surface is circled by dotted line. Fig. 18(a) is the fracture morphology of the specimen at 276 K. The orientations of fracture surfaces are random, only a small portion of the fracture surface line is parallel to the {110} orientation. As the temperature equals 313 K, a notable preference of {001} orientation is confirmed. However, a substantial increment in the {110} fracture surface is observed as the temperature equals 283 K. The most severe HE occurs at 283 K, followed by 276 K, and the least severe at 313 K in the
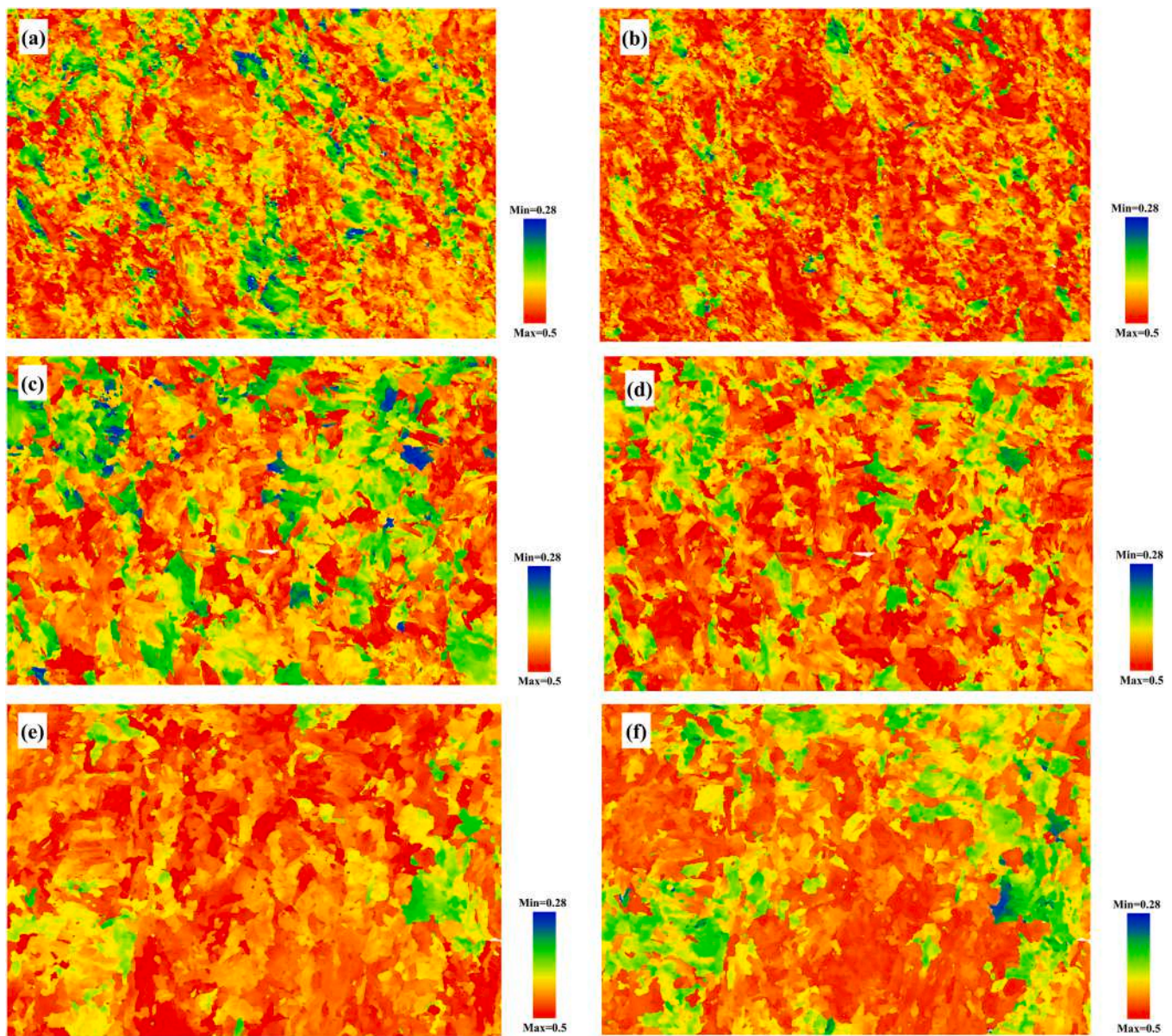
Fig. 19. Schmid Factor maps under different conditions: (a), (b) Schmid factor maps of {110}<111> and {112}<111> slip systems in the air at 295 K, respectively; (c), (d) Schmid factor maps of {110}<111> and {112}<111> slip systems with a current density of 20 mA/cm² at 313 K, respectively; (e), (f) Schmid factor maps of {110}<111> and {112}<111> slip systems with a current density of 20 mA/cm² at 283 K, respectively.

current three tests, as shown in Fig. 6(b). Also, the SEM images in Fig. 8 verify that the brittle fracture platform appears as the {110} orientation increases at the fracture surface.

To determine which slip band is preferential with increasing hydrogen concentration, the Schmid Factor maps beneath the failed surfaces are compared. The Schmid Factor plot of EBSD can be employed to interpret the texture evolution of the sample and identify the primary slip system where slip occurs [56]. The Schmid factor diagrams of {110}<111> and {112}<111> slip systems are illustrated in Fig. 19. The Schmidt factor exhibits a range of values from 0.28 to 0.5. The {110} and {112} planes in BCC metal structures exhibit relatively high Schmidt factors, ranging from 0.31 to 0.5 [57]. For the BCC crystal, we would thus expect yield/slip to first occur in grains whose {111} and {112} planes are oriented such that the angle between the applied force and the slip plane normal is 45°, and that the angle between the applied force and the slip direction is also 45°. According to the Schmidt factor formula: $m = \cos\theta\cos\Phi$ [58], the maximum Schmidt factor value would be 0.5. In this case, the dislocations in this slip direction on the slip

surface are favorable to occur. Therefore, in this study, we consider the theoretical value of 0.5 as the maximum value, while 0.28 is chosen as the minimum value within the suitable range of Schmidt factors for BCC structured metals. A bigger value indicates a higher probability of initiation of a specific dislocation slip system. In Fig. 19(a) and (b), the {110}<111> and {112}<111> dislocation densities beneath the fracture plane in air are characterized, respectively. The {110}<111> density is small because the ratio of the red region in (a) is not predominant. The probability of {112}<111> sliding is comparatively large since the color of the area is mainly red in (b). The {112}<111> dislocation is still preferable as the hydrogen charging current is 20 mA/cm² at 313 K. As the temperature is 283 K, the HE susceptibility is significant. When we compare (e) and (f), which indicated {110}<111> and {112}<111> initiation frequencies, the {110}<111> is the primary dislocation slip system because the red region in (e) is more remarkable than other temperatures. Data statistics regarding the occurrence frequencies of dislocation emission in different slip bands are shown in Fig. 20. The frequency of {110}<111> slip systems exhibit a
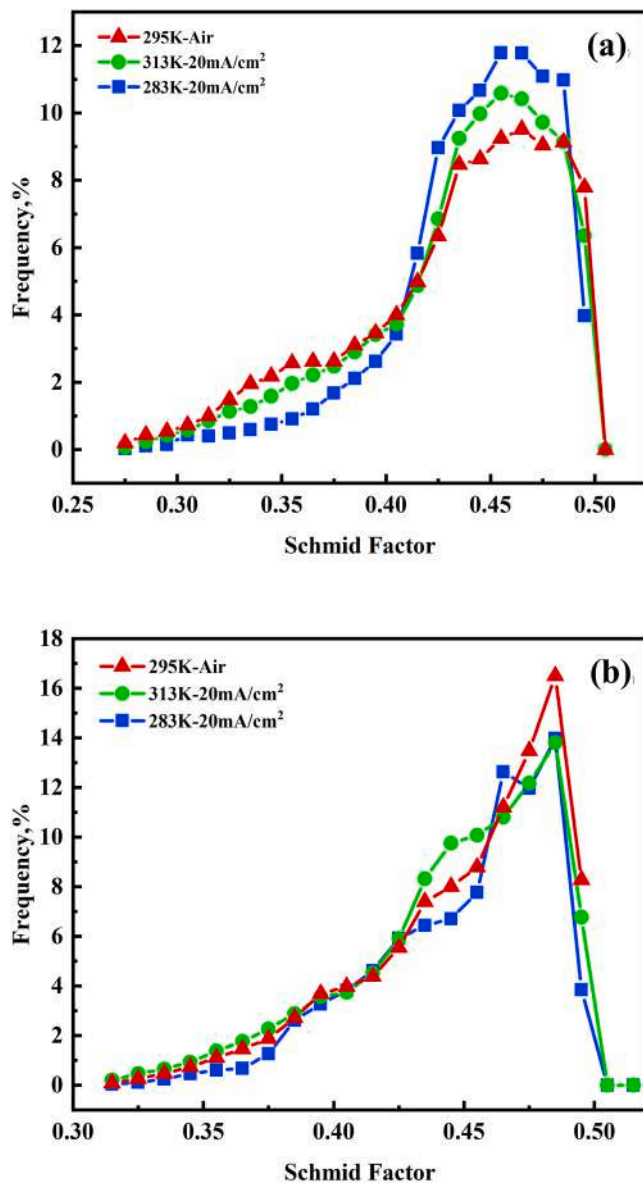
Fig. 20. Statistical analysis of Schmidt factors: (a) {110}<111> slip systems; (b) {112}<111> slip systems.

significant increase with increasing hydrogen concentration. Conversely, the frequency of {112}<111> slip system exhibits a slight decrease after hydrogen charging. Hydrogen atoms exist in tetrahedral sites between two {110} layers. According to the HEDE theory, the progressive increase in hydrogen concentration ultimately renders the {110}<111> slip systems more susceptible to sliding. However, hydrogen atoms exist in the {112} plane. The slipping of {112}<111> dislocation would be hindered [59,60].

5. Conclusion

The hydrogen-induced cracking of X70 steel is studied under different temperatures and hydrogen charging currents. The hydrogen concentration (C_o) calculated by the CC model could be used to quantify the susceptibility of HE. Based on current research, the existence of critical temperature to maximize the HE effect is also established.

We use the Arrhenius formula to characterize the hydrogen atom's adsorption behavior and Tafel slop to quantify the hydrogen molecule's desorption rate. The ratio of them (η) can elucidate the susceptibility of HE. There is a temperature to maximize the ratio. Thereby, this temperature is determined to be the critical temperature of HE. The expression of this critical temperature is also quantified as E_{ads}/R. However, if the hydrogen adsorption rate is maximized, e.g., the charging current is 30 mA/cm^2, only the hydrogen desorption rate is increased as temperature increases. The HE susceptibility is weakened by temperature. Generally, the maximum adsorption rate could never be satisfied in field operation. Hence, the HE sensitivity is constantly enhanced by charging currents, and the critical temperature should always exist.

Additionally, the fracture planes and dislocation slipping directions are analyzed with EBSD observation. As the hydrogen concentration increases, the fraction of {110} orientation increases on the fracture plane. Indicating that hydrogen atoms have a more significant effect on enhancing {110} orientation fracture. It should also be noted that hydrogen atoms could have distinct effects on different dislocation slipping systems. For instance, hydrogen concentration increment will enhance {110}<111> dislocation slipping system, while inhibiting the {112}<111> dislocations emission [59,60].

Author statement

We declare that this manuscript is original, has not been published before and is not currently being considered for publication elsewhere.

We confirm that the manuscript has been read and approved by all named authors and that there are no other persons who satisfied the criteria for authorship but are not listed. We further confirm that the order of authors listed in the manuscript has been approved by all of us.

CRediT authorship contribution statement

Zhiwen Pang: Writing – review & editing, Writing – original draft, Software, Investigation, Formal analysis, Data curation. **Hao Zhang:** Writing – review & editing, Writing – original draft, Methodology, Conceptualization. **Xiao Xing:** Writing – review & editing, Writing – original draft, Supervision, Methodology, Funding acquisition, Formal analysis, Conceptualization. **Jianguo Liu:** Writing – original draft, Formal analysis, Data curation. **Gan Cui:** Writing – original draft, Formal analysis, Data curation.

Declaration of Competing Interest

The authors declare that they have no known competing financial interests or personal relationships that could have appeared to influence the work reported in this paper.

Data availability

Data will be made available on request.

Appendix A. Supporting information

Supplementary data associated with this article can be found in the online version at doi:10.1016/j.corsci.2024.111939.

References

[1] R. Moradi, K.M. Groth, Hydrogen storage and delivery: Review of the state of the art technologies and risk and reliability analysis, Int. J. Hydrog. Energy 44 (2019) 12254–12269, https://doi.org/10.1016/j.ijhydene.2019.03.041.

[2] H. Barthelemy, M. Weber, F. Barbier, Hydrogen storage: Recent improvements and industrial perspectives, Int. J. Hydrog. Energy 42 (2017) 7254–7262, https://doi.org/10.1016/j.ijhydene.2016.03.178.

[3] I.M. Robertson, P. Sofronis, a Nagao, M.L. Martin, S. Wang, D.W. Gross, K.E. Nygren, Hydrogen Embrittlement Understood, Metall. Mater. Trans. A. 46 (2015) 2323–2341, https://doi.org/10.1007/s11661-015-2836-1.

[4] S.P. Lynch, Hydrogen embrittlement (HE) phenomena and mechanisms, Stress Corros. Crack. Theory Pr. (2011) 90–130, https://doi.org/10.1533/9780857093769.1.90.

[5] S.K. Dwivedi, M. Vishwakarma, Hydrogen embrittlement in different materials: A review, Int. J. Hydrog. Energy 43 (2018) 21603–21616, https://doi.org/10.1016/j.ijhydene.2018.09.201.

[6] J. Song, W. a Curtin, Atomic mechanism and prediction of hydrogen embrittlement in iron, Nat. Mater. 12 (2013) 145–151, https://doi.org/10.1038/nmat3479.

[7] C.D. Beachem, A new model for hydrogen-assisted cracking (hydrogen "embrittlement"), Metall. Trans. 3 (1972) 441–455, https://doi.org/10.1007/BF02642048.

[8] S. Hinotani, Y. Ohmori, F. Terasaki, Hydrogen crack initiation and propagation in pure iron single crysta, Mater. Sci. Technol. (U. Kingd.). 10 (1994) 141–148, https://doi.org/10.1179/mst.1994.10.2.141.

[9] D.P. Abraham, C.J. Altstetter, Hydrogen-enhanced localization of plasticity in an austenitic stainless steel, Metall. Mater. Trans. A. 26 (1995) 2859–2871, https://doi.org/10.1007/BF02669644.

[10] A. Kimura, H. Kimura, Hydrogen embrittlement in high purity iron single crystals, Mater. Sci. Eng. 77 (1986) 75–83, https://doi.org/10.1016/0025-5416(86)90355-1.

[11] S. Wang, K.E. Nygren, A. Nagao, P. Sofronis, I.M. Robertson, On the failure of surface damage to assess the hydrogen-enhanced deformation ahead of crack tip in a cyclically loaded austenitic stainless steel, Scr. Mater. 166 (2019) 102–106, https://doi.org/10.1016/j.scriptamat.2019.03.010.

[12] M.L. Martin, M. Dadfarnia, A. Nagao, S. Wang, P. Sofronis, Enumeration of the hydrogen-enhanced localized plasticity mechanism for hydrogen embrittlement in structural materials, Acta Mater. 165 (2019) 734–750, https://doi.org/10.1016/j.actamat.2018.12.014.

[13] H.K. Birnbaum, P. Sofronis, Hydrogen-enhanced localized plasticity-a mechanism for hydrogen-related fracture, Mater. Sci. Eng. A. 176 (1994) 191–202, https://doi.org/10.1016/0921-5093(94)90975-X.

[14] S. Wang, N. Hashimoto, Y. Wang, S. Ohnuki, Activation volume and density of mobile dislocations in hydrogen-charged iron, Acta Mater. 61 (2013) 4734–4742, https://doi.org/10.1016/j.actamat.2013.05.007.

[15] I.M. Robertson, The effect of hydrogen on dislocation dynamics, Eng. Fract. Mech. 68 (2001) 671–692.

[16] P. peng Bai, J. Zhou, B. wei Luo, S. qi Zheng, P. yan Wang, Y. Tian, Hydrogen embrittlement of X80 pipeline steel in H2S environment: Effect of hydrogen charging time, hydrogen-trapped state and hydrogen charging–releasing–recharging cycles, Int. J. Miner. Metall. Mater. 27 (2020) 63–73, https://doi.org/10.1007/s12613-019-1870-1.

[17] D.P. Williams, H.G. Nelson, Embrittlement of 4130 steel by low-pressure gaseous hydrogen, Metall. Trans. 1 (1970) 63–68.

[18] C.A. Zappfe, C.E. Sims, Hydrogen embrittlement, internal stress and defects in steel, Trans. Metall. Soc. AIME 145 (1941) 225–271.

[19] T. Zhang, W. Zhao, T. Li, Y. Zhao, Q. Deng, Y. Wang, W. Jiang, Comparison of hydrogen embrittlement susceptibility of three cathodic protected subsea pipeline steels from a point of view of hydrogen permeation, Corros. Sci. 131 (2018) 104–115, https://doi.org/10.1016/j.corsci.2017.11.013.

[20] T. Das, E. Legrand, S.V. Brahimi, J. Song, S. Yue, Evaluation of material susceptibility to hydrogen embrittlement (HE): An approach based on experimental and fi nite element (FE) analyses, Eng. Fract. Mech. (2019) 106714, https://doi.org/10.1016/j.engfracmech.2019.106714.

[21] T. Kanezaki, C. Narazaki, Y. Mine, S. Matsuoka, Y. Murakami, Effects of hydrogen on fatigue crack growth behavior of austenitic stainless steels, Int. J. Hydrog. Energy 33 (2008) 2604–2619, https://doi.org/10.1016/j.ijhydene.2008.02.067.

[22] AM Syrotyuk, I.M. Dmytrakh, Methods for the Evaluation of Fracture and Strength of Pipeline Steels and Structures Under the Action of Working Media. Part 2. Influence of Hydrogen-Containing Media, Mater. Sci. 50 (2015) 475–487, https://doi.org/10.1007/s11003-015-9745-8.

[23] L. Zhang, W. Cao, K. Lu, Z. Wang, Y. Xing, Y. Du, M. Lu, Effect of the cathodic current density on the sub-surface concentration of hydrogen in X80 pipeline steels under cathodic protection, Int. J. Hydrog. Energy 42 (2017) 3389–3398, https://doi.org/10.1016/j.ijhydene.2016.09.214.

[24] S. Wu, Z. Gao, D. Xia, M. Wu, Y. Liu, W. Hu, Effect of temperature on process and kinetic parameters of the hydrogen evolution reaction of X80 under CP, 3 (2021) 219–228, ⟨https://doi.org/10.1108/ACMM-12-2020-2413⟩.

[25] A.G. Oshchepkov, A. Bonnefont, V.N. Parmon, E.R. Savinova, Electrochimica Acta On the effect of temperature and surface oxidation on the kinetics of hydrogen electrode reactions on nickel in alkaline media, Electrochim. Acta 269 (2018) 111–118, https://doi.org/10.1016/j.electacta.2018.02.106.

[26] L. Jiang, M.J. Demkowicz, Surface coverage-limited hydrogen uptake into nickel under cathodic charging, Corros. Sci. 202 (2022) 110280, https://doi.org/10.1016/j.corsci.2022.110280.

[27] W. Wang, H. Fu, H. Zhang, Y. Yan, J. Li, Effect of Grain Orientation on Hydrogen Embrittlement Behavior of Interstitial-Free Steel, Met. (Basel) 12 (2022) 981.

[28] J. Hou, X. Kong, C.S. Liu, J. Song, Acta Materialia Hydrogen clustering in bcc metals: Atomic origin and strong stress anisotropy, Acta Mater. 201 (2020) 23–35, https://doi.org/10.1016/j.actamat.2020.09.048.

[29] D. Birenis, Y. Ogawa, H. Matsunaga, O. Takakuwa, Acta Materialia Interpretation of hydrogen-assisted fatigue crack propagation in BCC iron based on dislocation structure evolution around the crack wake, Acta Mater. 156 (2018) 245–253, https://doi.org/10.1016/j.actamat.2018.06.041.

[30] C.D. Beachem, Orientation of Cleavage Facets in Tempered Martensite (Quasi-cleavage) by Single Surface Trace Analysis Discussion of " Homogeneous Nucleation of CO Bubbles in, (1972).

[31] L. Cho, P.E. Bradley, D.S. Lauria, M.L. Martin, M.J. Connolly, J.T. Benzing, E.J. Seo, K.O. Findley, J.G. Speer, A.J. Slifka, Acta Materialia Characteristics and mechanisms of hydrogen-induced quasi-cleavage fracture of lath martensitic steel, Acta Mater. 206 (2021) 116635, https://doi.org/10.1016/j.actamat.2021.116635.

[32] A. Shibata, T. Murata, H. Takahashi, T. Matsuoka, N. Tsuji, Characterization of Hydrogen-Related Fracture Behavior in As-Quenched Low-Carbon Martensitic Steel and Tempered Medium-Carbon Martensitic, Metall. Mater. Trans. A. 46 (2015) 5685–5696, https://doi.org/10.1007/s11661-015-3176-x.

[33] A. Nagao, C.D. Smith, M. Dadfarnia, P. Sofronis, I.M. Robertson, The role of hydrogen in hydrogen embrittlement fracture of lath martensitic steel, Acta Mater. 60 (2012) 5182–5189.

[34] A. Shibata, Y. Momotani, T. Murata, T. Matsuoka, M. Tsuboi, N. Tsuji, Microstructural and crystallographic features of hydrogen-related fracture in lath martensitic steels, Mater. Sci. Technol. 33 (2017) 1524–1532.

[35] D. Wang, A.B. Hagen, P.U. Fathi, M. Lin, R. Johnsen, X. Lu, Materials Science & Engineering A Investigation of hydrogen embrittlement behavior in X65 pipeline steel under different hydrogen charging conditions, 860 (2022) ⟨https://doi.org/10.1016/j.msea.2022.144262⟩.

[36] F. Nakasato, I.M. Bernstein, F. Nakasato, Crystallographic and Fractographic Studies of Hydrogen-Induced Cracking in Purified Iron and Iron-Silicon Alloys, 9 (1978).

[37] R. Matsumoto, S. Taketomi, S. Matsumoto, N. Miyazaki, Atomistic simulations of hydrogen embrittlement, Int. J. Hydrog. Energy 34 (2009) 9576–9584, https://doi.org/10.1016/j.ijhydene.2009.09.052.

[38] A. Machová, G.E. Beltz, Ductile – brittle behavior of (0 0 1)[1 1 0] nano-cracks in bcc iron, 389 (2004) 414–418. ⟨https://doi.org/10.1016/j.msea.2003.11.089⟩.

[39] L. Ma, S. Xiao, H. Deng, W. Hu, Molecular dynamics simulation of fatigue crack propagation in bcc iron under cyclic loading, Int. J. Fatigue 68 (2014) 253–259, https://doi.org/10.1016/j.ijfatigue.2014.04.010.

[40] X. Xing, W. Chen, H. Zhang, Atomistic study of hydrogen embrittlement during cyclic loading: Quantitative model of hydrogen accumulation effects, Int. J. Hydrog. Energy 42 (2017) 4571–4578, https://doi.org/10.1016/j.ijhydene.2016.12.127.

[41] J. Song, W. a Curtin, A nanoscale mechanism of hydrogen embrittlement in metals, Acta Mater. 221 (2011) 1557–1569, https://doi.org/10.1016/j.actamat.2010.11.019.

[42] N. Boes, H. Züchner, Electrochemical methods for studying diffusion, permeation and solubility of hydrogen in metals, J. Less Common Met. 49 (1976) 223–240.

[43] L. Nanis, T.K.G. Namboodhiri, Mathematics of the electrochemical extraction of hydrogen from iron, J. Electrochem. Soc. 119 (1972) 691.

[44] J. Svoboda, G. Mori, A. Prethaler, F.D. Fischer, Determination of trapping parameters and the chemical diffusion coefficient from hydrogen permeation experiments, Corros. Sci. 82 (2014) 93–100, https://doi.org/10.1016/j.corsci.2014.01.002.

[45] X.Y. Cheng, H.X. Zhang, A new perspective on hydrogen diffusion and hydrogen embrittlement in low-alloy high strength steel, Corros. Sci. 174 (2020) 108800, https://doi.org/10.1016/j.corsci.2020.108800.

[46] A. Drexler, B. Helic, Z. Silvayeh, K. Mraczek, C. Sommitsch, J. Domitner, The role of hydrogen diffusion, trapping and desorption in dual phase steels, J. Mater. Sci. 57 (2022) 4789–4805, https://doi.org/10.1007/s10853-021-06830-0.

[47] X. Lu, D. Wang, R. Johnsen, Hydrogen diffusion and trapping in nickel-based alloy 625: An electrochemical permeation study, Electrochim. Acta 421 (2022) 1–11, https://doi.org/10.1016/j.electacta.2022.140477.

[48] T.K. Govindan Namboodhiri, L. Nanis, Concentration dependence of hydrogen diffusion in Armco iron, Acta Met. 21 (1973) 663–672, https://doi.org/10.1016/0001-6160(73)90075-8.

[49] E.C. Potter, The Mechanism of the Cathodic Hydrogen Evolution Reaction', (n.d.).

[50] T.J. Schmidt, P.N.R. Jr, N.M. Markovic, Temperature dependent surface electrochemistry on Pt single crystals in alkaline electrolytes: Part 2. The hydrogen evolution / oxidation reaction Temperature dependent surface electrochemistry on Pt single crystals in alkaline electrolytes Part 2. The, 0728 (2002). ⟨https://doi.org/10.1016/S0022-0728(02)00683-6⟩.

[51] E. Sciences, Temperature dependence of the Tafel slope for oxygen reduction on platinum in concentrated phosphoric acid*, 23 (1993) 597–605.

[52] C. Zhou, B. Ye, Y. Song, T. Cui, P. Xu, L. Zhang, Effects of internal hydrogen and surface-absorbed hydrogen on the hydrogen embrittlement of X80 pipeline steel, Int. J. Hydrog. Energy 44 (2019) 22547–22558, https://doi.org/10.1016/j.ijhydene.2019.04.239.

[53] A. Boda, S. Musharaf, ScienceDirect First principles DFT analysis on the diffusion kinetics of hydrogen isotopes through bcc iron (Fe): Role of temperature and surface coverage, Int. J. Hydrog. Energy 47 (2022) 31481–31498, https://doi.org/10.1016/j.ijhydene.2022.07.055.

[54] Z.S. Basinski, A.L. Sutton, The Lattice Expansion of Iron, (1955) 459–467. ⟨https://doi.org/10.1098/rspa.1955.0102⟩.

[55] S. Wang, S. Ohnuki, N. Hashimoto, K. Chiba, Materials Science & Engineering A Hydrogen effects on tensile property of pure iron with deformed surface, Mater. Sci. Eng. A 560 (2013) 332–338, https://doi.org/10.1016/j.msea.2012.09.075.

[56] Z. Yan, D. Wang, X. He, W. Wang, H. Zhang, P. Dong, Materials Science & Engineering A Deformation behaviors and cyclic strength assessment of AZ31B magnesium alloy based on steady ratcheting e ff ect, Mater. Sci. Eng. A 723 (2018) 212–220, https://doi.org/10.1016/j.msea.2018.03.023.

[57] V. Khademi, T.R. Bieler, C.J. Boehlert, On the correlation between plastic strain and misorientation in polycrystalline body-centered-cubic microstructures with an emphasis on the grain size, loading history, and crystallographic orientation, Int. J. Plast. 146 (2021) 103084, https://doi.org/10.1016/j.ijplas.2021.103084.

[58] D. Hull, D.J. Bacon, Introduction to dislocations, Elsevier,, 2011.

[59] X. Xing, F. Li, J. Liu, G. Cui, Z. Li, Y.F. Cheng, Molecular dynamics modeling of hydrogen-induced plastic deformation and cracking of α-iron, J. Mater. Sci. Technol. 176 (2024) 119–131.

[60] Z. Wang, X. Shi, X.S. Yang, W. He, S.Q. Shi, X. Ma, Atomistic simulation of the effect of the dissolution and adsorption of hydrogen atoms on the fracture of α-Fe single crystal under tensile load, Int. J. Hydrog. Energy 46 (2021) 1347–1361, https://doi.org/10.1016/j.ijhydene.2020.09.216.